A micro–meso–model of intra–laminar fracture in fiber–reinforced composites based on a Discontinuous Galerkin/Cohesive Zone Method

L. Wu[a], D. Tjahjanto[b,c], G. Becker[a,1], A. Makradi[d], A. Jérusalem[b,e], L. Noels[a,*]

[a]University of Liège - Computational & Multiscale Mechanics of Materials, Chemin des Chevreuils 1, B-4000 Liège, Belgium
[b]IMDEA Materials Intitute, C/ Eric Kandel 2, 28906 Getafe, Spain
[c]Department of Solid Mechanics, KTH Royal Institute of Technology, SE-100 44, Stockholm, Sweden
[d]Centre de Recherche Public Henri Tudor, Avenue John F. Kennedy, 29, L-1855 Luxembourg, G.D. of Luxembourg
[e]University of Oxford, Department of Engineering Science, Parks Road, OX1 3PJ, UK

Abstract

The recently developed hybrid discontinuous Galerkin/extrinsic cohesive law framework is extended to the study of intra–laminar fracture of composite materials. Toward this end, micro–volumes of different sizes are studied. The method captures the debonding process, which is herein proposed to be assimilated to a damaging process, before the strain softening onset, and the density of dissipated energy resulting from the damage (debonding) remains the same for the different studied cell sizes. Finally, during the strain softening phase a micro–crack initiates and propagates in agreement with experimental observations. We thus extract a resulting mesoscale cohesive law, which is independent on the cell sizes, using literature methods.

Keywords: Composites, fracture, debonding, cohesive law, microscale, discontinuous Galerkin method

*Corresponding author, Phone: +32 4 366 48 26, Fax: +32 4 366 95 05
Email address: L.Noels@ulg.ac.be (L. Noels)
[1]PhD candidate at the Belgian National Fund for Education at the Research in Industry and Farming

1. Introduction

The engineering fracture theories developed for homogeneous materials cannot always be directly applied when considering new engineered heterogeneous materials, such as composites. Indeed, fracture mechanisms of composites are complex and require a multiscale approach: from the microscale within a ply to the laminate macroscale. Although some numerical solutions have been developed to address these particular topics, such as the damage–based micro–meso–macro approaches for composites proposed by Ladevèze et al. [1], or a purely numerical approaches as discussed by LLorca et al. [2], it is still challenging to predict explicitly the composite fracture behavior using microscale simulations.

One way to predict a mesoscale fracture criterion from numerical simulations at the microscale is to analyze the microscale deformation mechanisms using finite elements combined to models accounting for the fracture processes ranging from micro–crack initiation to micro–crack propagation. A natural way to achieve this goal is to enhance the finite–element model with the so–called cohesive zone method (CZM).

The cohesive zone method was pioneered by Barenblatt [3] and Dugdale [4] to introduce traction between crack lips during the separation process. In particular in Barenblatt's model the traction separation law (TSL) decreases monotonically until reaching zero at a critical opening Δ_c to model a progressive damage of the material. The energy dissipated during this process corresponds to the fracture energy G_C, see Figure 1(c) for an example of cohesive law. Because of its physical background, *i.e.* for quasi–brittle materials the TSL is related to the breaking of atomic bonding, of its simple characterization by two physical parameters, *i.e.* the material strength σ_c and the fracture energy G_C, and of its relatively straightforward implementation, see Figure 1(a), the CZM is widely used to model fracture.

The first practical implementation was proposed by Hillerborg et al. [5] by introducing a cohesive element to integrate the TSL between two finite elements where a crack can potentially initiate or propagate, see Figure 1(a). In most of applications of the CZM for finite elements, the cohesive elements are inserted at the beginning of the simulation, in which case the TSL should also model the reversible fracture stage. Such TSLs are called intrinsic cohesive laws and are illustrated in Figure 1(b). In this figure it can be seen that the law is decomposed into an initial reversible part followed by an irreversible decreasing law, once the stress reaches the material strength σ_c. If
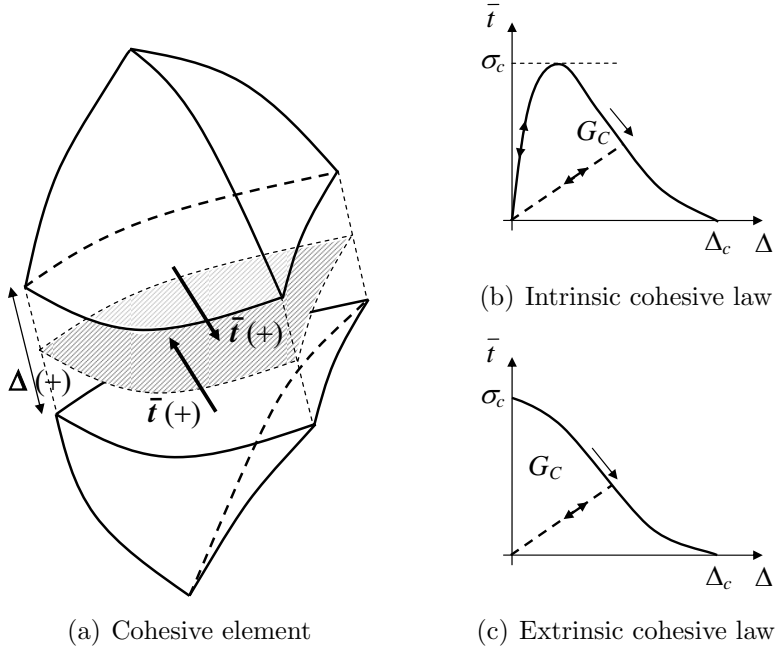
Figure 1: Implementation of the cohesive zone model (CZM): (a) Cohesive element inserted between two bulk elements to integrate the Traction Separation Law (TSL) linking the opening $\boldsymbol{\Delta}$ to the surface traction $\bar{\boldsymbol{t}}$; (b) Intrinsic TSL, which includes the pre–fracture (reversible) stage; (c) Extrinsic TSL, which models the fracture stage only. The cohesive laws are characterized by the strength σ_c, the critical opening Δ_c and the critical energy release rate G_C. A single arrow is used to indicate the irreversible parts of the TSLs, and a double arrow is used for the reversible parts.

unloading happens during this irreversible stage the law becomes reversible again, but with a reduced elastic stiffness associated to damage. This CZM is attractive as it can easily be implemented, in particular when the crack path is well defined, *e.g.* for debonding [6, 7, 8], material interface decohesion [9, 10], structure interface decohesion [11, 12, 13], composite delamination [14, 12, 15, 16] *etc* ... Studies have also been conducted to determine the shape of the TSL under mixed modes loading [17, 18] or to account for ductility of materials [19]. The macroscale TSL for crystals can also be deduced from atomistic considerations, see [20] *e.g.*

As the intrinsic cohesive law has been proved to be an efficient and accurate tool to simulate a crack initiation and propagation at *a priori* defined interfaces it is tempting to apply the method to model or to predict fracture

3

in homogeneous phases, such as in the matrix phase of composites, by inserting cohesive elements in–between all bulk elements. Unfortunately, Xu and Needleman [21] have shown that such a scheme not only exhibits a strong mesh dependency but also alters the structural stiffness. Indeed the intrinsic CZM does not satisfy the consistency condition – due to the initial slope in the reversible part of the cohesive law, see Figure 1(b) – adding spurious stiffness elements in a mesh dependent way. Although this error can be reduced by increasing the initial slope of the TSL [14, 22, 23] this leads to an ill–conditioned stiffness matrix for static simulations or to unacceptable small values of the critical time step for explicit dynamic simulations [24].

In order to avoid the drawbacks inherent to the intrinsic approach, Camacho and Ortiz [25] and Ortiz et al. [26] proposed the use of an extrinsic cohesive law, see Figure 1(c), which models only the irreversible part of the response. Practically the simulation proceeds with a classical finite element approach and cohesive elements are introduced at the interface of bulk elements at the onset of fracture. Although the 3D implementation of this framework [27] is not straightforward due to the mesh topology changes during the computation, it predicts crack propagation with an energy and a crack path that both converge with the mesh size[2], as shown by Arias et al. [28] and by Molinari et al. [29]. However the implementation complexity increases drastically for parallel framework [30] and can suffer from low scalability unless a graph–based internal structure is used [31, 32].

These difficulties probably explain why the cohesive zone model was mainly used for composites analyzes in the intrinsic form, thus reducing the applicability to cases for which the crack path is well defined, *e.g.* delamination [14, 12, 15, 16], debonding [6, 7], and interface failure [11, 12, 13]. However the cohesive approach remains attractive to simulate the failure of composites at the microscale as it is characterized by measurable physical values only, *i.e.* the strength σ_c and the fracture energy G_C for the matrix, the fibers, and at the interface. Additionally the CZM can account for anisotropic and elasto–plastic behaviors in a straightforward way, allowing the models of the different phases to be as accurate as needed. Finally the CZM does not require the preexistence of a crack as it can detect the initiation process, allowing debonding process and micro–crack propagation to be considered simultaneously. Some alternatives exist to model fracture as the

---

[2]For unstructured meshes

4

xFEM approach [33, 34] or the embedded localization method [35], which can also be combined with a cohesive approach, see the overview by de Borst et al. [36].

Recently an hybrid discontinuous Galerkin/cohesive zone model (DG / CZM) has been suggested by Mergheim et al. [37] and developed by Radovitzky et al. [38] and by Prechtel et al. [39]. The main feature of the DG method for non–linear solid mechanics [40, 41, 42, 43, 44] is its ability to take into account discontinuities of the unknown field between bulk elements. In the associated weak formulation the integration by part is realized on the elements leading to element interface terms ensuring the continuity and compatibility of the solution in a stable and consistent way. With the hybrid DG/CZM method, interface elements are therefore inserted between bulk elements at the beginning of the simulation and continuity during the pre–fracture stage is ensured by having recourse to the consistent DG interface terms. An extrinsic cohesive law can thus be integrated on the already existing interface elements once a fracture criterion is met, without requiring mesh topology changes. This approach has been successfully implemented in a 3D parallel framework by Radovitzky et al. [38] to solve fragmentation problems with ultra–fine meshes. The method has also been used by Prechtel et al. [39] in 2D to study the effect of the fiber shapes on the composite resistance. Such an approach has also been developed for thin homogeneous elastic bodies by Becker et al. [45, 46] and for thin homogeneous elasto–plastic structures by Becker and Noels [47] with success.

This paper presents an hybrid DG/extrinsic cohesive law framework extended to the study of composite failures at the microscale. Toward this end, micro–structures of unidirectional (UD) carbon–fiber reinforced epoxy matrix are discretized using the DG/CZM approach and submitted to a transverse loading. From identification of the parameters of the matrix (elasto–plastic material law, strength σ_c and fracture energy G_C), of the fibers (transversely isotropic material law, strength σ_c, and fracture energy G_C), and of the interface (strength σ_c, and fracture energy G_C), direct numerical simulations are conducted on characteristic micro–volumes to predict the failure behavior of the homogenized material. The components material behaviors are extracted from the manufacturer data sheets when possible, and/or from literature when needed. As these analyzes require extensive computations on refined meshes a new parallel form of the DG/CZM based on "ghost elements" is developed in this paper following the approach developed for shells by Becker and Noels [47]. The framework can thus deliver results in a reduced

computational time. This implementation if more efficient than the parallel framework developed by Noels and Radovitzky [42] as less information is exchanged between the processors.

During the fracture process the representativeness of the characteristic volume becomes ambiguous as the crack tends to localize [48, 49, 50, 51, 52]. Moreover the extracted homogenized response should still converge with respect to the RVE size, which is not straightforward to obtain in case of discontinuities happening at the micro–level [49, 50, 53]. Despite these difficulties Verhoosel et al. [54] have proposed a way to extract a corresponding mesoscopic cohesive law from the computations of micro–structures involving fracture modeled by cohesive elements. To do so the elastic and plastic deformations are subtracted from the boundary displacement in order to extract the mesoscopic crack opening. They have demonstrated the convergence of the multiscale analyzes with respect to the size of the microscopic problem in the absence of irreversible behaviors before the onset of the mesoscopic crack.

In the present work characteristic micro–volumes or cells of different sizes, and thus of different fibers numbers, are considered. When using the DG/CZM framework multiple cracks can initiate, bifurcate or merge. This approach is thus able to capture the debonding process occuring *prior* to the onset of a dominant crack propagation in the matrix phase of the micro–structure. We additionally show that the failure behavior can be divided into two phases. Before the strain softening onset the failure process is shown to be mainly driven by debonding, and this is assimilated to a damaging process in the material. It is shown that the density of dissipated energy resulting from this damage is the same for the different cell sizes. During the strain softening phase a micro–crack propagates in the cell, and is assimilated at the mesoscale to a meso–crack propagation. The method proposed by Verhoosel et al. [54] is then used to extract a corresponding mesoscale cohesive law by considering the modification of the elastic properties of the composite material due to debonding. In particular it is shown that the extracted law is the same for the different cell sizes even when only a few fibers are considered. The predicted behavior is then compared to experimental results obtained from laminate tests. The behaviors *prior* to catastrophic failure of the tensile samples are found to be in good agreement. Nguyen et al. [55] proposed a computational homogenization framework based on the same principle. Before strain softening onset the bulk response of the cell is homogenized, and a meso–crack is introduced at strain softening onset,

6

and the homogenization proceed with a continuous–discontinuous homogenization framework. However a non–local damage model for the matrix is considered in their micro–model, while in the present work we use a cohesive zone method at that scale.

The paper is organized as follows. In Section 2 the DG/CZM method is explained and the main equations are derived. As the efficiency of the method is a key element for its practical application, the implementation in parallel is briefly reported in Section 3. Finally the application of the developed framework to the failure study of a transversely loaded UD composite is reported in Section 4, with a view towards multi–scale applications. It is shown in this section that a cell with a reduced number of fibers can be used to predict the debonding process happening *prior* to the strain softening onset and the crack propagation during the strain softening phase.

2. Combined discontinuous Galerkin/extrinsic cohesive law framework

In the following the DG approach for solid mechanics is first recalled. Although deformations of composites remain small at the mesoscale the framework follows a large deformation approach. Indeed at the microscale the displacements and possibly the rotations of the elements are not negligible compared to their size during the crack opening, which does not allow a small displacement assumption. The formulation of the DG/extrinsic cohesive law framework is then summarized.

2.1. DG formulation

Let $\Omega_0 \subset \mathbb{R}^3$ be a body subjected to a force per unit mass $\mathbf{B}$. Its boundary surface Γ_0 includes two parts: the Dirichlet boundary denoted by Γ_{0D}, where the displacement $\boldsymbol{u}$ is prescribed by $\bar{\boldsymbol{u}}$, and the Neumann boundary denoted by Γ_{0T}, where the traction is prescribed by $\mathbf{T}$. One always has $\Gamma_0 = \Gamma_{0D} \cup \Gamma_{0T}$ and $\Gamma_{0D} \cap \Gamma_{0T} = \emptyset$. The continuum equations stated in the material form are

$$\rho_0 \ddot{\boldsymbol{u}} = \boldsymbol{\nabla}_0 \cdot \mathbf{P}^T + \rho_0 \mathbf{B} \quad \text{in } \Omega_0 \,, \tag{1}$$

$$\boldsymbol{u} = \bar{\boldsymbol{u}} \quad \text{on } \Gamma_{0D} \,, \text{ and} \tag{2}$$

$$\mathbf{P}\boldsymbol{N} = \mathbf{T} \quad \text{on } \Gamma_{0T} \,. \tag{3}$$

In these relations ρ_0 is the initial density, $\mathbf{P}$ is the first Piola–Kirchhoff stress tensor, and $\boldsymbol{N}$ is the outward unit surface normal in the reference configuration. For the uncracked body the exact solution $\boldsymbol{u}^{\text{exact}} \in \mathbf{H}^2$ of the strong

7

form (1-3) is continuous, and so its derivative. So considering any uncracked surface in the body $\Gamma_{0U} \in \Omega_0$ implies

$$\llbracket \boldsymbol{u}^{\text{exact}} \rrbracket = 0 \quad \text{on} \quad \Gamma_{0U} \,, \tag{4}$$

$$\llbracket \mathbf{P}^{\text{exact}} \rrbracket = 0 \quad \text{on} \quad \Gamma_{0U} \,. \tag{5}$$

In these equations we have considered the jump operator. This jump operator and the average operator are defined on an interface of two parts of the body, arbitrarily denoted "plus" and "minus", by respectively

$$\llbracket \bullet \rrbracket = \left[\bullet^+ - \bullet^- \right] \quad \text{and} \quad \langle \bullet \rangle = \frac{1}{2} \left[\bullet^+ + \bullet^- \right] \,. \tag{6}$$

The case of cracked interfaces will be considered in the next subsection.

The finite element discretization of the body Ω_0 is expressed as $\Omega_0 = \bigcup_e \bar{\Omega}_0^e$, where $\bar{\Omega}_0^e$ is the union of the open domain Ω_0^e with its boundary Γ_0^e. Here the symbol Ω_0 is used to represent the body and its discretization for simplicity. The weak form of Equations (1-3) arises by seeking a polynomial approximation $\boldsymbol{u}$ of the displacement field over the discretization Ω_0. Contrarily to a continuous Galerkin approximation, which requires $\boldsymbol{u} \in C^0 \left(\Omega_0 \right)$, the DG approach only requires an element–wise continuous polynomial approximation, $i.e.$ $\boldsymbol{u} \in C^0 \left(\Omega_0^e \right)$. Consequently, for a DG formulation the trial functions $\boldsymbol{w}_u$ are also discontinuous across the element interfaces on the internal boundary of the body $\Gamma_{0I} = \left[\bigcup_e \Gamma_0^e \right] \backslash \Gamma_0$.

The new weak formulation of the problem is obtained in a similar way as for the continuous Galerkin approximation. The linear momentum balance is enforced in a weighted–average sense by multiplying the strong form (1) by a suitable test function $\boldsymbol{w}_u$ and by integrating by parts in the domain. However, since both test and trial functions are discontinuous, the integration by parts is not performed over the whole domain but on each element instead. Using traditional DG considerations, see [40] $e.g.$ for details, this leads to

$$\int_{\Omega_0} \left(\rho_0 \ddot{\boldsymbol{u}} \cdot \boldsymbol{w}_u + \mathbf{P} : \boldsymbol{\nabla}_0 \boldsymbol{w}_u \right) dV + \int_{\Gamma_{0I}} \llbracket \boldsymbol{w}_u \rrbracket \cdot \langle \mathbf{P} \rangle \cdot \boldsymbol{N}^- dS$$
$$= \int_{\Omega_0} \rho_0 \mathbf{B} \cdot \boldsymbol{w}_u dV + \int_{\Gamma_{0T}} \boldsymbol{w}_u \cdot \mathbf{T} dS \,. \tag{7}$$

where $\boldsymbol{N}^-$ is the outward unit surface normal of the "minus" element. In this equation, the discretized stress tensor $\mathbf{P}$ results from the discretized

deformation gradient state $\mathbf{F} = \boldsymbol{\nabla}_0\boldsymbol{u} + \mathbf{I}$ through a constitutive material law, see Section Appendix A.

In the formulation (7), neither the inter–element displacement continuity is enforced, nor the stability of the method. The compatibility equation $\boldsymbol{u}^- - \boldsymbol{u}^+ = 0$ on $\Gamma_{0\mathrm{I}}$ is enforced through a so–called symmetrization term in $[\![\boldsymbol{u}]\!]$ and a (sufficiently large) quadratic stabilization term in $[\![\boldsymbol{u}]\!]$ and $[\![\boldsymbol{w}_u]\!]$. With the addition of the quadratic terms, the general displacement jumps are stabilized in the numerical solution, while the symmetrization term leads to an optimal convergence rate with respect to the mesh size. The large deformation material response is thus properly considered for the final weak formulation of the problem, which consists of finding $\boldsymbol{u}$ such that

$$
\int_{\Omega_0} (\rho_0 \ddot{\boldsymbol{u}} \cdot \boldsymbol{w}_u + \mathbf{P} : \boldsymbol{\nabla}_0\boldsymbol{w}_u)\, dV + \int_{\Gamma_{0\mathrm{I}}} [\![\boldsymbol{w}_u]\!] \cdot \langle \mathbf{P} \rangle \cdot \boldsymbol{N}^- dS +
$$

$$
\int_{\Gamma_{0\mathrm{I}}} \left\{ [\![\boldsymbol{w}_u]\!] \otimes \boldsymbol{N}^- : \langle \frac{\beta_s}{h_s} \mathbb{C} \rangle : [\![\boldsymbol{u}]\!] \otimes \boldsymbol{N}^- \right\} dS +
$$

$$
\int_{\Gamma_{0\mathrm{I}}} \left\{ [\![\boldsymbol{u}]\!] \cdot \langle \mathbb{C} : \boldsymbol{\nabla}_0\boldsymbol{w}_u \rangle \cdot \boldsymbol{N}^- \right\} dS =
$$

$$
\int_{\Omega_0} \rho_0 \mathbf{B} \cdot \boldsymbol{w}_u\, dV + \int_{\Gamma_{0\mathrm{T}}} \boldsymbol{w}_u \cdot \mathbf{T}\, dS \,, \tag{8}
$$

where h_s is the mesh size and where β_s is the penalty parameter for stabilization. For elasto–plastic materials, the Lagrangian tangent moduli $\mathbb{C}$ used for the symmetrization and stabilization terms cannot vanish for perfectly–plastic behaviors [42]. Thus a neo–Hookean expression of $\mathbb{C}$ is considered. This formulation, known as the Interior Penalty Method, has been shown to be stable (for $\beta_s > 10$). There also exist implementations of the extrinsic cohesive law resulting from a variational process [56], which do not require an Interior Penalty Method as the continuity of displacements results from a minimization process. Also, for explicit dynamic time integrations, the DG method reduces the critical time step by a factor of $\sqrt{\beta_s}$ as compared to a continuous Galerkin (CG) formulation [42].

The DG formulation is completed by a material model, which is transversely isotropic elastic for the fibers, and follows a J_2–elastic–plastic model for the matrix. These models are formulated in the non–linear large deformation framework and are reported in Appendix A.

More details about the DG formulation can be found in [40, 42].

2.2. Hybrid DG/CZM

Considering a cracked surface inside the body $\Gamma_C \in \Omega$ in its deformed configuration, the equations (1-5) governing the strong form are completed in terms of the surface traction $\bar{\boldsymbol{t}} = \boldsymbol{\sigma} \cdot \boldsymbol{n}$ in the deformed configuration, where $\boldsymbol{\sigma}$ is the Cauchy stress tensor and where $\boldsymbol{n}$ is the deformed unit normal outward to any of the two lips.[3] The new equations of the strong form are

$$[\![\bar{\boldsymbol{t}}]\!] = 0 \quad \text{on} \quad \Gamma_C\,, \tag{9}$$

$$\bar{t} = \|\bar{\boldsymbol{t}}\| \leq \bar{t}_{\max} \quad \text{on} \quad \Gamma_C\,, \tag{10}$$

$$(\bar{t}_{\max} - \bar{t}) > 0 \text{ if } \dot{\Delta}^* < 0 \text{ or } \Delta^* < \Delta^*_{\max} \quad \text{on} \quad \Gamma_C\,, \tag{11}$$

$$(\bar{t}_{\max} - \bar{t}) = 0 \text{ if } \dot{\Delta}^* > 0 \text{ and } \Delta^* = \Delta^*_{\max} \quad \text{on} \quad \Gamma_C\,, \tag{12}$$

where $\bar{t}$ represents the surface traction amplitude between the crack lips, where Δ^* is the opening of the crack, and where $\bar{t}_{\max}$ is the surface traction amplitude at the maximum crack opening $\Delta^*_{\max}$ reached during the fracture process.
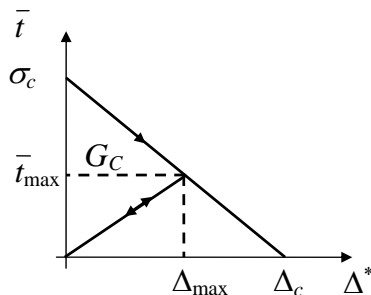

Figure 2: Linear extrinsic TSL $\bar{t}$ in terms of the effective opening Δ^*. If unloading occurs, the TSL follows a reversible path that consists of a line segment connecting the origin with $(\Delta^*_{\max}, \bar{t}_{\max})$. σ_c, Δ^*_C and $G_C = \frac{\Delta^*_c \sigma_c}{2}$ are respectively the strength, the critical effective opening, and the critical energy release rate of the TSL.

The cohesive model (9-12) is now particularized to the linear TSL developed by Camacho and Ortiz [25], and by Pandolfi and Ortiz [30], and

---

[3]One can always expressed the equations either in the reference configuration using the Piola stress tensor $\mathbf{P}$ and the reference normal $\boldsymbol{N}$ or in the deformed configuration using the Cauchy stress tensor $\boldsymbol{\sigma}$ and the normal in the deformed configuration $\boldsymbol{n}$. For the cohesive model it is easier to consider the deformed configuration and Nanson's formula gives the relation between the surface traction in both configurations.

illustrated in Figure 2. The crack nucleation at an interface element is governed by an effective cohesive stress

$$\sigma_{\text{eff}} = \begin{cases} \sqrt{\sigma^2 + \beta^{-2}\tau^2} & \text{if} \quad \sigma \geqslant 0 \\ \frac{1}{\beta} \ll |\tau| - \eta|\sigma| \gg & \text{if} \quad \sigma < 0 \end{cases}, \tag{13}$$

where $\sigma = \boldsymbol{n} \cdot \bar{\boldsymbol{t}}$ and $\tau = \sqrt{\bar{\boldsymbol{t}} \cdot \bar{\boldsymbol{t}} - \sigma^2}$ are respectively the normal and tangent components of the surface traction $\bar{\boldsymbol{t}}$ at the interface. The parameter $\beta = \frac{K_{IIC}}{K_{IC}}$ assigns different weights to the mode I and mode II crack opening, η is the friction coefficient of the material, and the operator $\ll \bullet \gg$ refers to the positive value, *i.e.* zero in case the argument is negative. Equation (13) implicitly accounts for the different behaviors of the material under tension and compression. However in this paper we do not consider fracture in compression. Once, the effective cohesive stress reaches the critical effective strength, *i.e.* $\sigma_{\text{eff}} \geqslant \sigma_{\text{c}}$ the fracture initiates and the TSL is used to evaluate the traction $\bar{\boldsymbol{t}}$ between the crack lips.

The effective surfaces separation Δ^* is evaluated from the surface opening vector $\boldsymbol{\Delta}^*$ by

$$\Delta^* = \sqrt{\ll \Delta_{\text{n}}^* \gg^2 + \beta^2 \Delta_{\text{t}}^{*2}}, \tag{14}$$

where Δ_{n}^* is the separation along the interface element normal $\boldsymbol{n}$ in the deformed configuration, and where Δ_{t}^* is the separation along the interface element tangent $\boldsymbol{t}$ in the deformed configuration. The effective surfaces separation has a superscript "*" as the initial opening $[\![\boldsymbol{u}_0]\!]$, which exists at fracture onset due to the weak continuity enforcement of the DG formulation, has to be subtracted from the real opening $[\![\boldsymbol{u}]\!]$ to ensure continuity at fracture initiation:

$$\begin{cases} [\![\boldsymbol{u}]\!]^* = [\![\boldsymbol{u}]\!] - [\![\boldsymbol{u}]\!]_0 \\ \Delta_{\text{n}}^* = [\![\boldsymbol{u}]\!]^* \cdot \boldsymbol{n} \\ \Delta_{\text{t}}^* = [\![\boldsymbol{u}]\!]^* \cdot \boldsymbol{t} \end{cases}. \tag{15}$$

The tangential direction is evaluated from $\boldsymbol{t} = \frac{[\![\boldsymbol{u}]\!]^* - \Delta_{\text{n}}^*\boldsymbol{n}}{\|[\![\boldsymbol{u}]\!]^* - \Delta_{\text{n}}^*\boldsymbol{n}\|}$ during opening.

The linear cohesive law, shown in Figure 2, includes an irreversible softening part during the crack opening and a reversible part if a crack unloading occurs. In the latter, the reversible path consists in a line segment which connects the origin with the point corresponding to the maximum opening

11

reached $(\Delta^*_{\max}, \bar{t}_{\max})$. The effective cohesive traction can then be computed from

$$\bar{t} = \sigma_c \left(1 - \tfrac{\Delta^*}{\Delta_c} \right) \qquad \text{for } \dot{\Delta}^* \geqslant 0, \text{ and } \Delta^* = \Delta_{\max}, \tag{16}$$

$$\bar{t} = \bar{t}_{\max} \tfrac{\Delta^*}{\Delta_{\max}} \qquad \text{for } \dot{\Delta}^* < 0, \text{ or } \Delta^* < \Delta_{\max}. \tag{17}$$

However, for small $\Delta_{\max}$ a reversible unloading is not allowed in order to avoid instabilities in the explicit time integration.

Finally the cohesive traction vector $\bar{\boldsymbol{t}}$ can be evaluated as a function of the effective cohesive traction $\bar{t}$, following

$$\bar{\boldsymbol{t}} = \bar{t} \left(\tfrac{\Delta^*_n}{\Delta^*} \boldsymbol{n} + \beta \tfrac{|\Delta^*_t|}{\Delta^*} \boldsymbol{t} \right) \qquad \text{for } \sigma \geqslant 0, \tag{18}$$

$$\bar{\boldsymbol{t}} = \bar{t} \beta \tfrac{|\Delta^*_t|}{\Delta^*} \boldsymbol{t} \qquad \text{for } \sigma < 0. \tag{19}$$

Note that at fracture initiation as the effective opening is zero, the ratio $\frac{\Delta^*_n}{\Delta^*}$ and the ratio $\frac{|\Delta^*_t|}{\Delta^*}$ are respectively initialized to $\frac{\sigma_0}{\sigma_c}$ and $\frac{\tau_0}{\beta\sigma_c}$, with σ_0 the normal part of the surface traction at fracture initiation and with τ_0 the tangential part of the surface traction at fracture initiation, see Eq. (13). Indeed these values ensure the traction continuity between the uncracked and cracked configurations as, using Eqs. (13) and (18), the tension at transition is $\bar{t} = \|\bar{\boldsymbol{t}}\| = \sigma_c$, which corresponds to the amplitude of the surface traction at fracture initiation.

In the DG framework described in Section 2.1, the DG surface terms are integrated using interface elements, see Figure 1(a), and the onset of fracture can be detected by the use of a fracture stress criterion as in the extrinsic CZM approach. When a crack nucleates at an interface element, the DG terms are substituted by a TSL, which models the fracture process. Hence, if $\bar{\boldsymbol{t}}^-$ is the surface traction evaluated on the minus side, and resulting from the TSL in the deformed configuration, the weak form (8), which was holding for bodies without cracked surfaces only, becomes in the more general setting

$$\int_{\Omega_0} \left(\rho_0 \ddot{\boldsymbol{u}} \cdot \boldsymbol{w}_u + \mathbf{P} : \boldsymbol{\nabla}_0 \boldsymbol{w}_u \right) dV + \int_{\Gamma_I} \alpha \bar{\boldsymbol{t}}^- \left([\![\boldsymbol{u}]\!] \right) \cdot [\![\boldsymbol{w}_u]\!] \, ds +$$

$$\int_{\Gamma_{0I}} (1-\alpha) [\![\boldsymbol{w}_u]\!] \cdot \langle \mathbf{P} \rangle \cdot \boldsymbol{N}^- dS + \int_{\Gamma_{0I}} (1-\alpha) [\![\boldsymbol{u}]\!] \cdot \langle \mathbb{C} : \boldsymbol{\nabla}_0 \boldsymbol{w}_u \rangle \cdot \boldsymbol{N}^- dS$$

$$+ \int_{\Gamma_{0I}} (1-\alpha) [\![\boldsymbol{w}_u]\!] \otimes \boldsymbol{N}^- : \langle \tfrac{\beta_s}{h_s} \mathbb{C} \rangle : [\![\boldsymbol{u}]\!] \otimes \boldsymbol{N}^- dS$$

$$= \int_{\Omega_0} \rho_0 \mathbf{B} \cdot \boldsymbol{w}_u dV + \int_{\Gamma_{0T}} \boldsymbol{w}_u \cdot \mathbf{T} dS, \tag{20}$$

12

where a binary operator α is defined as $\alpha = 0$ before the fracture onset and as $\alpha = 1$ after the fracture stress criterion is met on Γ_I. In this expression as the traction $\bar{\boldsymbol{t}}^-$ predicted by the TSL is usually in the deformed configuration with the deformed infinitesimal surface ds, the integration of this term is written in the current configuration as opposed to the other interface terms.

Unlike the extrinsic CZM no modification of the mesh is required during the shift procedure from the uncracked ($\alpha = 0$) to a cracked ($\alpha = 1$) configuration, and only the constitutive formulations at the interface elements are modified. This makes the hybrid DG/CZM easy to be implemented in an existing parallel code, and ensures a high scalability of the parallel simulations. Another advantage of the DG/CZM is its ability to account for partially fractured interface elements since both cracked ($\alpha = 1$) and uncracked ($\alpha = 0$) quadrature points are simultaneously allowed within each interface element.

At uncracked quadrature points ($\alpha = 0$), the DG formulation prevents in a weak way the penetration of elements, in the same way as it prevents the opening. At cracked quadrature points ($\alpha = 0$), before total opening of the crack ($\Delta^* < \Delta_c$), the penetration in compression ($\Delta_n^* < 0$) is constrained using a penalty term. For simplicity, this has been achieved by interpolating the unloading curve of the TSL, see Figure 2, in the negative values. Once the cracked quadrature point is fully opened ($\Delta^* \geq \Delta_c$) a contact algorithm should be considered as relative displacements on both sides of the crack can be consequent. However, based on the fact that only monotonous loading conditions are considered here, this last one has not been implemented in the code. In the variational extrinsic cohesive law formulation [56] the non–penetration condition is satisfied from the minimization process.

One of the advantage of the DG/CZM is its ability to consider a wide range of non-linear bulk material behaviors, that can be combined with a TSL. Another advantage of this approach is that it respects the consistency in the pre-fracture stage contrarily to the intrinsic CZM, which suffers from severe restrictions in the critical time step size and/or from artificial compliance.

More details on this hybrid method can be found in [38, 57].

3. Efficient parallel implementation

In this work the hybrid DG/CZM framework presented in the previous section is used to study crack propagation at the microscale. In order for the method to predict meaningful results refined meshes will have to be

considered. As extensive computations will be required a new parallel implementation, based on "ghost elements", was developed for DG applications by Becker and Noels [47] and is considered herein. This method is highly scalable, and easily implementable in a finite-element code. After having established the finite element expression of the weak form its parallel implementation in Gmsh, a mesher developed by Geuzaine and Remacle [58], is briefly explained.

3.1. Finite element discretization and explicit time integration

The weak formulation (20) of the DG/CZM framework is taken as the basis for the finite element discretization. The displacement mapping and the arbitrary trial functions are approximated by an interpolation in each element Ω_0^e following, respectively,

$$\boldsymbol{u}(\boldsymbol{X}) = \sum_{a=1}^{N} N_a(\boldsymbol{X})\boldsymbol{u}_a, \quad \text{and} \quad \boldsymbol{w}_u(\boldsymbol{X}) = \sum_{a=1}^{N} N_a(\boldsymbol{X})\delta\boldsymbol{u}_a, \qquad (21)$$

where N_a is the traditional shape function corresponding to the node $a \in \{1, ..., N\}$, where N is the number of nodes and where $\boldsymbol{u}_a$ is the current nodal displacements vector. In the presented framework the displacement field, the arbitrary trial functions, and the shape functions are discontinuous across elements interfaces.

Applying the discretization process, the finite-element forces can be computed, see Appendix B for details, and the weak form (20) reduces to a set of ordinary differential equations to be integrated in the time interval T:

$$\sum_{b=1}^{N} \mathbf{M}_{ab}\ddot{\boldsymbol{u}}_b + \mathbf{f}_{\text{int}a}(\boldsymbol{u}) + \mathbf{f}_{\text{I}a}(\boldsymbol{u}) = \mathbf{f}_{\text{ext}a} \quad \forall t \in T, \qquad (22)$$

where $\mathbf{M}$ is the discretized mass matrix, $\mathbf{f}_{\text{int}}$ is the discretized internal forces vector, $\mathbf{f}_{\text{I}}$ is the discretized interface forces vector, and where $\mathbf{f}_{\text{ext}}$ is the discretized external forces vector. The set of Equations (22) is completed by the initial conditions $\boldsymbol{u}_a(t=0) = \mathbf{x}_a(t=0) - \boldsymbol{X}_a = 0$ and $\dot{\boldsymbol{u}}_a(t=0) = \mathbf{v}_{0a}$, where $\mathbf{v}_{0a}$ are the initial nodal velocities.

The dynamics equation (22) is integrated using an explicit time integration. The scheme considered herein is the second-order accurate Hulbert–Chung time integration [59], which exhibits numerical dissipation. The time

interval of interest T is discretized into time steps and the integration is accomplished through an incremental solution procedure in each time intervals $[t^n, t^{n+1}]$. As this integration is conditionally stable the time step should satisfy $\Delta t = t^{n+1} - t^n < \Delta t_{\mathrm{crit}}$, where Δt_{crit} has been reduced by $\sqrt{\beta_s}$ to account for the DG space-discretization. Knowing the solution at time t^n, the solution at time t^{n+1} can be obtained by the expressions

$$\ddot{\boldsymbol{u}}_b^{n+1} = \frac{1}{1 - \alpha_M} \sum_{b=1}^{N} \mathbf{M}_{ab}^{-1}[\mathbf{f}_{\mathrm{ext}a}^n - \mathbf{f}_{\mathrm{int}a}^n - \mathbf{f}_{\mathrm{I}a}^n] - \frac{\alpha_M}{1 - \alpha_M} \ddot{\boldsymbol{u}}_b^n, \qquad (23)$$

$$\dot{\boldsymbol{u}}_b^{n+1} = \dot{\boldsymbol{u}}_b^n + \Delta t[1 - \gamma_M]\ddot{\boldsymbol{u}}_b^n + \Delta t \gamma_M \ddot{\boldsymbol{u}}_b^{n+1}, \text{ and} \qquad (24)$$

$$\boldsymbol{u}_b^{n+1} = \boldsymbol{u}_b^n + \Delta t \dot{\boldsymbol{u}}_b^n + \Delta t^2[\frac{1}{2} - \beta_M]\ddot{\boldsymbol{u}}_b^n + \Delta t^2 \beta_M \ddot{\boldsymbol{u}}_b^{n+1}, \qquad (25)$$

where the parameters α_M, β_M and γ_M are defined according to the desired numerical dissipation[4], see [59] for more details.

3.2. Parallel implementation

The time-integration is performed in parallel using the METIS library [60] to partition the mesh for multi-processors, see Figures 3(a)-3(b). Currently mesh refinements are only possible before partitioning and are not performed during the simulation.

Each processor solves the boundary value problem corresponding to its own partition of the mesh and in particular the internal forces $\mathbf{f}_{\mathrm{int}}$ of the bulk elements and the interface forces $\mathbf{f}_{\mathrm{I}}$ of the interface elements belonging to the partition. The continuity between the partitions is ensured through the interface elements existing at processors boundaries.

In order to evaluate the interface forces $\mathbf{f}_{\mathrm{I}}$ at processors boundaries, each processor defines the ghost elements, which are the elements of neighboring partitions sharing the same interface, see Figure 3(b). In this way each processor can thus create the interface elements at partition interfaces and compute the related interface force $\mathbf{f}_{\mathrm{I}}$. Since at the interface of ghost elements the interface terms are computed in two partitions, only the part (interface

---

[4]To be stable, a time integration algorithm must either conserve the system energy or dissipate part of it during a time–step computation. Depending on the selected parameters, the Hulbert–Chung algorithm either conserves the energy or numerically dissipates its higher frequencies contributions. In the latter, this so–called numerical dissipation stabilizes the simulation as oscillations related to the purely numerical modes are damped.
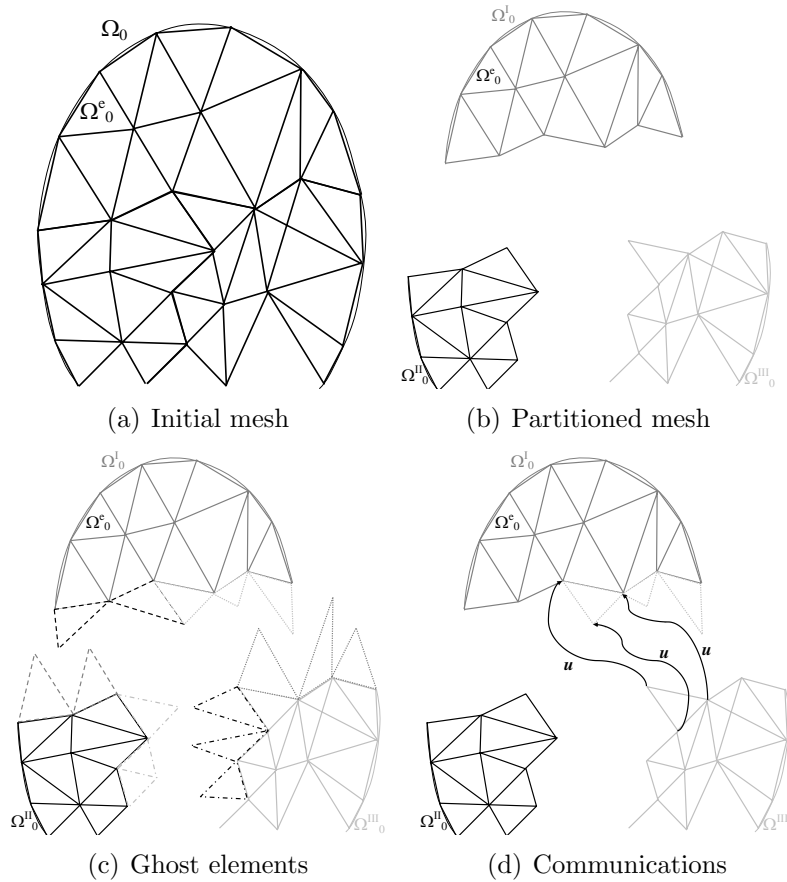
Figure 3: 2D view of the parallel implementation of the DG/CZM (a) Initial mesh of the body Ω_0 discretized into elements Ω_0^e before partitioning (TSL). (b) Meshes in the partitions Ω_0^i. (c) Ghost elements on each partition in dotted lines. (d) Communications required at each time step to exchange the nodal displacements $\boldsymbol{u}$.

force $\mathbf{f}_I^+$ or $\mathbf{f}_I^-$) on the boundary belonging to the processor is assembled into the local $\mathbf{f}_I$ vector.

However for the interface forces at partitions boundaries to be correctly evaluated on each processor, the ghost elements should always have the correct deformation state, which requires their nodal values to be communicated from the original element through the network via Message Passing Interface (MPI), the standardized and portable message-passing system for parallel computing, see Figure 3(d). These are the only communications required by the method, which is not more expensive than usual "reduce" operations of

parallel implementations.

This suggested implementation is more efficient than the parallel DG formulation previously suggested by Noels and Radovitzky [42] since it avoids the communication of values computed from the material law (stress tensors, Hooke tensors, *etc*) when integrating the forces for the interface elements between partitions. It therefore leads to a reduced number of communications (only one per time step, communicating the nodal values of ghost elements). Compared to the node–based ghost parallel implementation–meaning that ghost bulk elements are the ones sharing a node with elements in other partitions–of the extrinsic cohesive law proposed in [61], our method is a face–based ghost implementation–meaning that ghost bulk elements are the ones sharing a face with elements in other partitions. This simplification, which reduces the communication mapping, is possible with the DG/ECL framework because instead of duplicating the nodes our implementation is based on the duplication of the degrees of freedom.

4. Application

In this section the behavior of a UD carbon-fiber reinforced epoxy matrix under transverse loading is studied. The material is made of prepreg Hexply M10.1/38%/UD300/HS (R)[5], which contains 38% of M10.1 epoxy resin by weight and 62% of high strength carbon fibers UD300/CHS by weight. The final composite has a fiber volume fraction of 60% after curing[6].

The components material behaviors are extracted from the manufacturer data sheets when possible and/or from literature when needed. Direct numerical simulations are conducted on characteristic micro-volumes of different sizes, and thus of different fibers numbers, to predict the failure behavior of the homogenized material. The predicted behavior is also compared to experimental results obtained from laminate tests.

4.1. Computational Model

Three cells of increasing fibers number, $2{\times}2$, $4{\times}4$ and $8{\times}8$, whose sections are represented in Figure 4, are considered to study the transverse fracture of the composite. The UD fibers have a diameter of 10.4 μm. The size of a cell is proportional to the number of fibers included $L_8 = 2L_4 = 4L_2 = 8 \times 12.79$

---

[5]http://www.hexcel.com/Resources/DataSheets/Prepreg-Data-Sheets/M101_eu.pdf
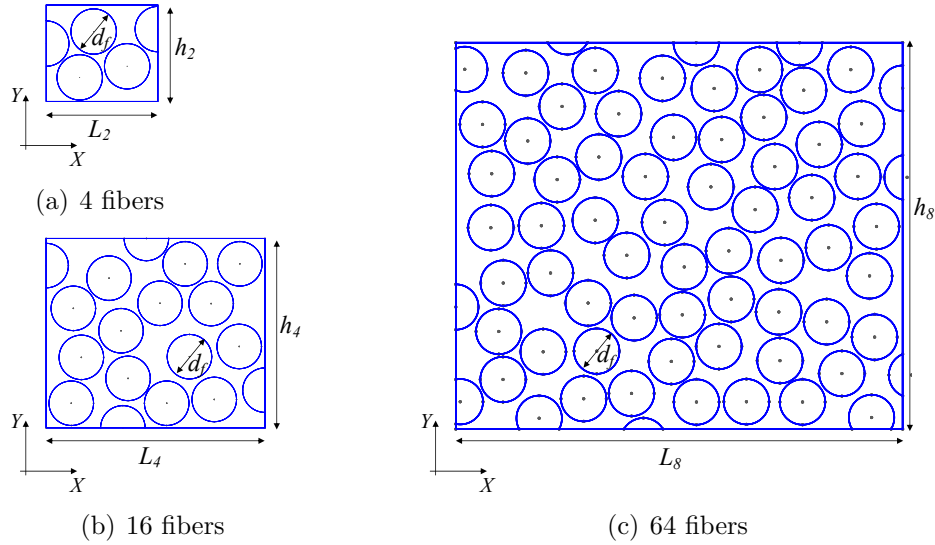[6]The percentage is obtained from a microscopic imaging process of the cured laminates

Figure 4: 2D view of the studied cells. The fibers diameter d_f is constant and the length L_k and height h_k of the $k \times k$–fiber cell are proportional to the number of fibers: $L_8 = 2L_4 = 4L_2$ and $h_8 = 2h_4 = 4h_2$. The thickness is constant for all the cells.

μm and $h_8 = 2h_4 = 4h_2 = 8 \times 11.073$ μm, which leads to 60% fiber volume ratio. The thickness of the cells is $t = 1.04$ μm. The boundary conditions are illustrated in Figure 5. The displacement of the right boundary is denoted by $\boldsymbol{u}^{\mathrm{m}}$. As discussed by Coenen et al. [51, 52], traditional periodic boundary conditions cannot be used to study localization in a cell as they would modify the way such a localization occurs. In this paper we study a transverse failure and it is reasonable to think that the crack should propagate in an average direction perpendicular to the loading, in which case the boundary conditions applied are consistent.

The Hulbert–Chung [59] time integration algorithm described in Section 3.1 is considered, with numerical dissipation in order to minimize the dynamic effects[7]. The cells are transversely loaded in the X-direction at a constant rate of 3 m/s, which is an optimum rate to obtain a quasi-static solution in a reasonable computational time. The recourse to an explicit (dynamic) scheme, even if a quasi-static solution is expected, is justified in order to

---

[7]The spectral radius at bifurcation of the time integration algorithm is set to zero, see [59] for details
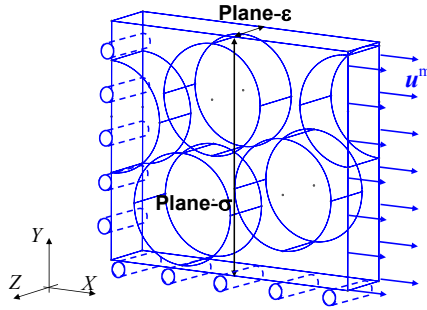
18

Figure 5: Description of the boundary conditions applied to the cells subjected to a controlled microscale displacement $\boldsymbol{u}^m$ along X.

avoid the convergence problems induced by the introduction of cracks.

The cells are meshed with 4,437, 9,723 and 38,733 quadratic tetrahedra for respectively the 2×2, 4×4 and 8×8-fiber cells. Only one element layer is considered on the thickness.

All the numerical results are presented and compared to the experimental ones in Section 4.4.

4.2. Material properties
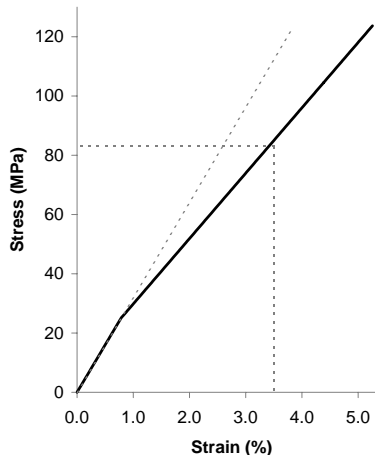
Figure 6: Tensile stress–strain curve predicted with the considered elasto–plastic model for the epoxy matrix. The linear response, the tensile strength, and the maximum tensile strain given by the manufacturer are reported in dotted lines.

19

Table 1: Material properties of the composite components. Dashed lines correspond to manufacturer data.

Property of carbon fibers	Value
Density ρ [kg/m^3]	1750
Longitudinal Young's modulus E_L [GPa]	230
Transverse Young's modulus E_T [GPa]	40
Transverse Poisson ratio ν_TT [-]	0.20
Longitudinal-Transverse Poisson ration ν_LT [-]	0.256
Transverse shear modulus G_TT [GPa]	16.7
Longitudinal-Transverse shear modulus G_LT [GPa]	24
Property of epoxy matrix	Value
Density ρ [kg/m^3]	1000
Young's modulus E [GPa]	3.2
Poisson ratio ν [-]	0.3
Initial yield stress σ_Y [MPa]	25
Hardening modulus h [GPa]	7.1

The carbon fibers are assumed to be linear elastic and transversely isotropic. Typical material constants for T300 carbon fibers are considered and are reported in Table 1 [62, *e.g*]. The cured epoxy matrix properties reported by the manufacturer are a tensile modulus of 3.2 GPa and a tensile strength of 83 MPa at 3.5% strain. By lack of elasto-plastic data a linear hardening law

$$R(p) = hp\,, \tag{26}$$

in terms of the equivalent plastic strain p, is considered with the material properties reported in Table 1. The corresponding tensile stress–strain curve of the epoxy matrix is illustrated on Figure 6, where the known manufacturer data are also reported.

The properties of the cohesive model at the interfaces are taken from the literature and reported in Table 2. The critical strength σ_c of the epoxy is provided by the supplier. For the interface matrix / fiber, the resistance is generally lower, and a value $\sigma_c = 45$MPa is chosen, as it will be shown it predicts the correct strength of the composite material. A typical value for the epoxy fracture energy G_C is of the order of 100 J/m^2 [63, 64]. The

Table 2: Material properties of the interfaces.

Intra-epoxy property	Value
Strength σ_c [MPa]	83
Critical energy release rate G_C [J/m^2]	78
Fracture mode toughness ratio β [-]	0.87
Intra-carbon fiber property	Value
Strength σ_c [MPa]	3600
Critical energy release rate G_C [J/m^2]	100
Fracture mode toughness ratio β [-]	0.87
Epoxy/carbon fiber property	Value
Strength σ_c [MPa]	45
Critical energy release rate G_C [J/m^2]	100
Fracture mode toughness ratio β [-]	0.87

literature also reports values of a few hundreds J/m^2 for fiber pull-out [65]. Therefore we choose arbitrarily a value of 78 J/m^2 for the epoxy matrix, slightly lower than the value of 100 J/m^2 for the interface with the fibers. As the fibers have a tensile strength provided by the suppliers much higher, the values of G_C has no influence on the results since only the transverse fracture is studied and is thus chosen arbitrarily high. In order to avoid "blow–up"[8] during the simulations a statistical distribution with 20% margin is used on the cohesive strength σ_c as suggested in [66].

4.3. Experiments

The specimens were manufactured from 8 layers of the prepreg Hexply M10.1/38%/UD300/HS (R). The prepreg was cured at 120º C during 60 min under an applied pressure of 0.4 MPa. The resulting thickness of the specimen is 2.15 mm ± 0.02 mm. In order to test the transverse fracture [90x]-laminated specimens were used for the tensile tests. Specimens were cut from an autoclave consolidated UD laminate panel of 300×300 mm^2 and their geometry schematic is shown in Figure 7. The direction of the

---

[8]"Blow–up" occurs when all the faces of one or many elements open at the same time in which case these elements can become free. For example this could happen under uniform tension if the strength of the all interface quadrature points is the same.
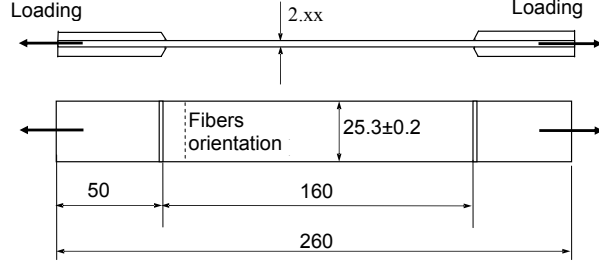
Figure 7: Geometry schematics of the 90º tensile specimen (units in mm).The directions of the fibers and of the loading are also reported.

fibers are also reported. To prevent gripping damage aluminum tabs were glued at both extremities of each specimen. The static tensile tests were carried out on a 1185 nº H4573(ME002) Instran machine in displacement control mode with a constant cross-head speed of 2 mm/min, according to the specification of ISO-527-4 standard. The loading direction is illustrated on Figure 7. Five specimens were used for the tensile tests up to fracture and the strain was measured with a strain gauge. Finally the Young's modulus E_{T}, failure strength σ_f, and strain ε_f in 90º direction were obtained.

4.4. Results

Table 3: Apparent energy release rate.

Model	$G_{\max} - G\vert_{\sigma_f}$ from Figure 8(e)	$\int_0^\infty \bar{t}d\Delta$ from Figure 11(b)
2×2 fibers	121.63 J/m^2	122.27 J/m^2
4×4 fibers	122.7 J/m^2	121.8 J/m^2
8×8 fibers	121 J/m^2	121.2 J/m^2

During the numerical simulations the right boundary of the studied cells is subjected to a X-displacement u^{m} and the reaction force $\mathrm{f_{ext}}$ is recorded. Figures 8(a) and 8(b) present the evolution of the extracted stress ($\sigma_k = \mathrm{f}_{\mathrm{ext}\,k}/(h_k t_k)$, where h_k and t_k are respectively the height and thickness of the $k \times k$-fiber cell), with respect to the extracted strain ($\epsilon_k = u_k^{\mathrm{m}}/L_k$, where L_k is the length of the $k \times k$-fiber cell). In the previous equations and subsequently the subscript "k" associated to $\mathrm{f}_{\mathrm{ext}}$ and u^{m} (as well as ρ_D and G in the following) refers to the respective $k \times k$–fiber cell. The experimental results,

22

(a) Stress *vs.* strain (b) Zoom

(c) Density of energy released (d) Zoom
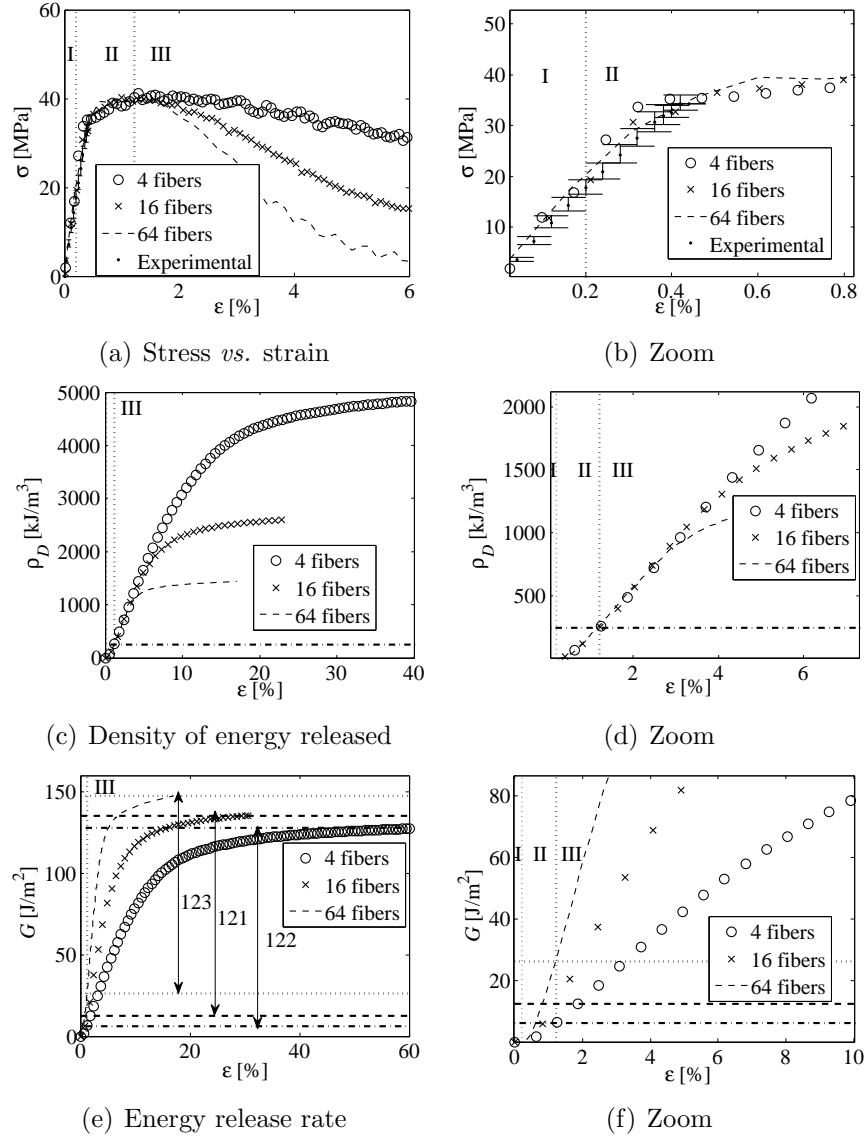
(e) Energy release rate (f) Zoom

Figure 8: Results of the numerical simulations separated in three zones: zone I is the elastic response, zone II is the damaging stage, and zone III corresponds to the crack propagation stage. (a) and (b) Stress (σ)-strain (ε) curves extracted from the unit cells. (c) and (d) Density of energy released during the process ρ_D. (e) and (f) Energy release rate during the process G. The reported values are the deduced critical energy release rates G_C for the different cells.
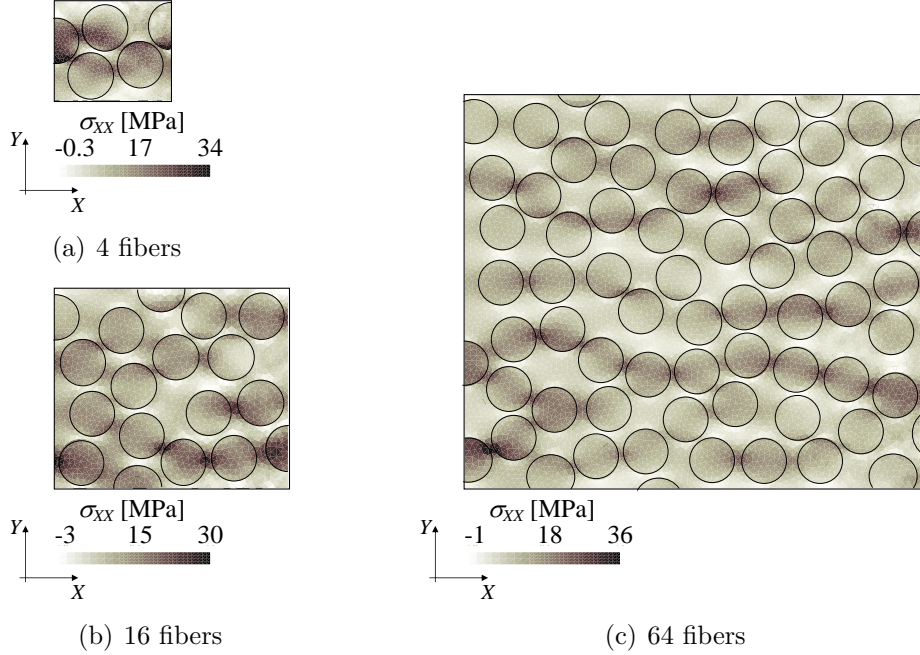
(a) 4 fibers

(b) 16 fibers

(c) 64 fibers

Figure 9: Distribution of stress along X (σ_{XX}) on the cells during the elastic process (Stage I) at $\varepsilon_{XX} = 0.11\%$.

with their deviations, are also reported on the curves. One can observe three stages in the cell response:

- Zone I: Elastic stage. For deformations lower than 0.2% the response is purely elastic. The results are independent of the cell size and match the experimental results. Figure 9 represents the stress distribution in the different cells at a 0.11%-strain state.

- Zone II: Damaging stage. Fibers debonding occurs for deformations between 0.2% and about 1.2% and some energy is released due to this debonding process. The dissipated energy density evolution ρ_D is reported on Figure 8(c), with

$$\rho_{D\,k} = \frac{W_{\text{ext}\,k} - K_k - W_{\text{int}\,k}}{L_k h_k t_k}, \qquad (27)$$

where L_k, h_k and t_k are respectively the length, height and thickness of the $k \times k$-fiber cell, and where $W_{\text{ext}\,k}$, K_k and $W_{\text{int}\,k}$ are respectively the
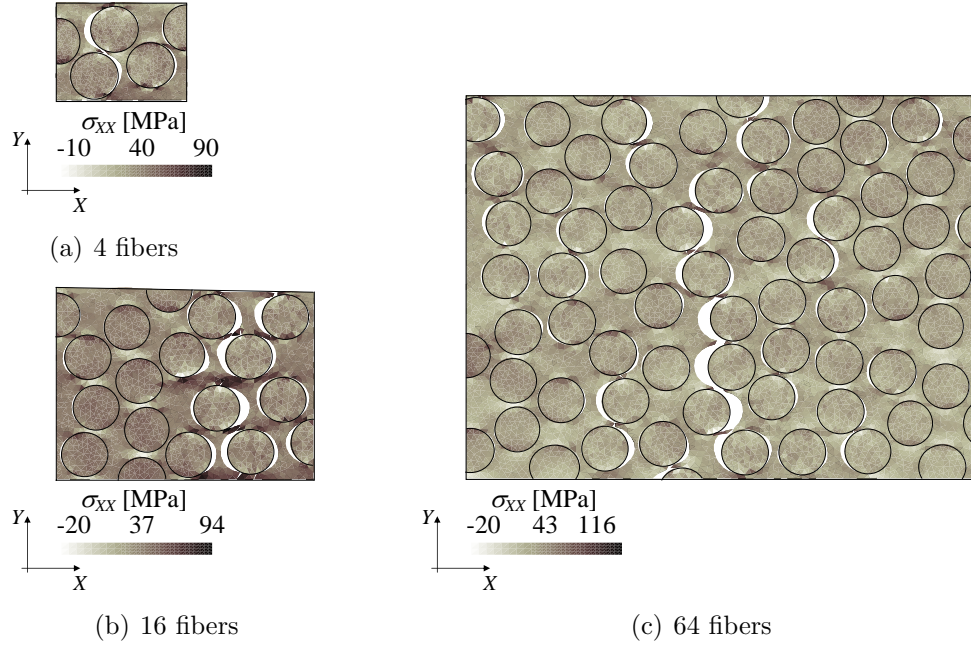
24

(a) 4 fibers

(b) 16 fibers

(c) 64 fibers

Figure 10: Distribution of stress along X (σ_{XX}) on the cells at strain softening onset (end of Stage II). Displacements are magnified by 10.

work of external forces, the kinetic energy, and the work of the internal forces. Clearly this energy density is similar for the different cell sizes until the stress reaches 1.2%, which is the strain softening point[9]. At that point a dominant crack has eventually formed in the matrix and the stress reaches a maximum value σ_f. During the debonding process associated to a damaging process an energy of about 248 kJ/m^3 is released. During this stage the response in terms of strain is not sensitive to the cell size. Figure 10 represents the stress distribution in the different cells at σ_f.

- Zone III: Crack propagation stage. If the strain keeps increasing one main crack propagates in the cell linking the debonding zones. During this strain softening response no response could be measured during the experiments as the samples tested have a size much larger than the

---

[9]Due to the numerical oscillations in the stress responses determining the softening point from the stress *vs* strain curves is less accurate than from this divergence point
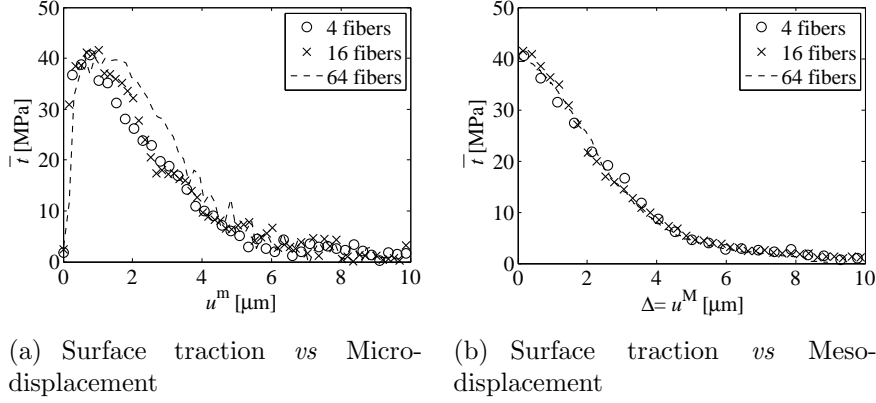
(a) Surface traction *vs* Micro-displacement

(b) Surface traction *vs* Meso-displacement

Figure 11: Extracted cohesive law. (a) Extracted surface traction $\bar{t}$ *vs* displacement of the cells u_k^{m}. (b) Extracted traction $\bar{t}$ *vs* extracted meso–displacement u_k^{M} following the work of Verhoosel et al. [54].

critical opening of the cohesive zone, inducing an unstable fracture. Figure 8(e) represents the evolution of the energy release rate G, which is the energy released per unit cell area during the crack propagation

$$G_k = \frac{W_{\mathrm{ext}\,k} - K_k - W_{\mathrm{int}\,k}}{h_k t_k} \ . \tag{28}$$

The differences of energy release rate between the softening point and the end of the fracture process are extracted from Figure 8(e) for the different cell sizes and converge to the apparent critical energy release rate G_{C} of the composite. Indeed, the values obtained for the different cells are reported in Table 3, were it can be seen that the discrepancy is lower than 2%. At the end of the process, the release energy rate is independent with the cell sizes. However during that stage, the response depends on the cell size. Indeed the strain-stress curves, see Figure 8(a), and the stress evolution in terms of the cell boundary displacement u^{m}, see Figure 11(a), depend on the cell size. In order to extract a cohesive law from the micro–response on a studied cell Verhoosel et al. [54] derived energetically consistent relations for quasi-brittle solids which can be summarized as follows:

1. The cohesive traction $\bar{\boldsymbol{t}}$ is directly obtained from the boundary forces

$$\bar{\boldsymbol{t}} = \frac{\sum_{a=1}^{N} \mathbf{f}_{\mathrm{ext}\,a}}{ht} \ , \tag{29}$$

26

(a) 4 fibers

(b) 16 fibers

(c) 64 fibers

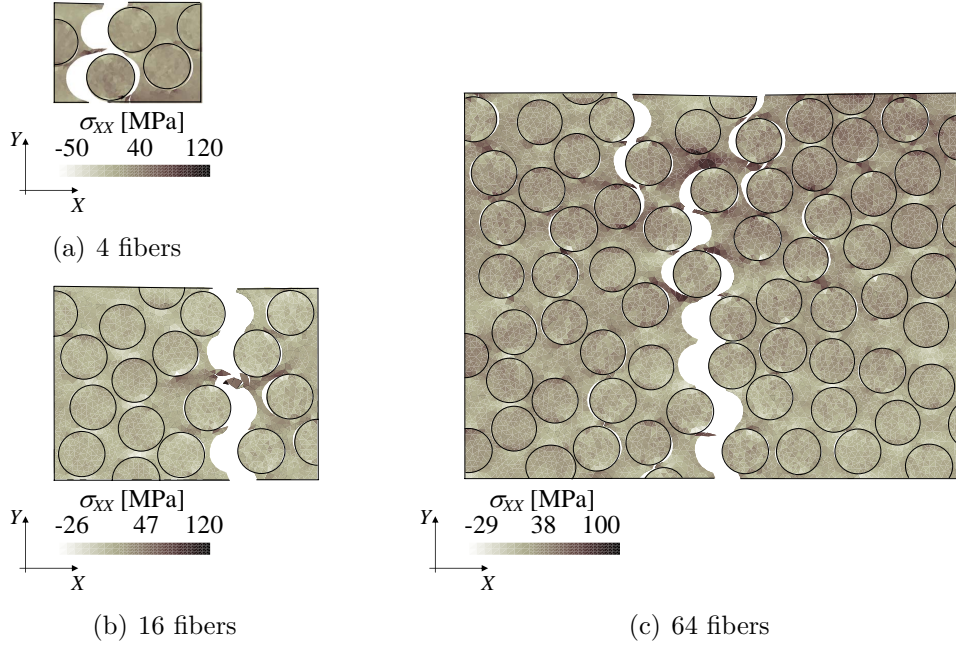Figure 12: Distribution of stress along X (σ_{XX}) on the cells during crack opening (Stage III) at $\Delta = 1\mu$m. Displacements are magnified by 5.

where h and t are respectively the height and thickness of the cell.

2. The mesoscopic opening variation $\delta\boldsymbol{u}^{\mathrm{M}}$ can be deduced from the microscopic boundary displacement $\delta\boldsymbol{u}^{\mathrm{m}}$ following

$$\delta\boldsymbol{u}^{\mathrm{M}} = \delta\boldsymbol{u}^{\mathrm{m}} - L\mathcal{G}_0 : \boldsymbol{e}_X \otimes \boldsymbol{e}_X \cdot \delta\bar{\boldsymbol{t}} - \delta\boldsymbol{u}_0^{\mathrm{m}} , \qquad (30)$$

where $\mathcal{G}_0$ is the elastic compliance tensor, L is the cell length, and where

$$\delta\boldsymbol{u}_0^{\mathrm{m}} = L \left(\mathcal{G} - \mathcal{G}_0\right) : \boldsymbol{e}_X \otimes \boldsymbol{e}_X \cdot \delta\bar{\boldsymbol{t}} , \qquad (31)$$

accounts for the change in the compliance tensor $\mathcal{G}$ due to irreversible behaviors as plasticity.

In this paper we assume that the plastic deformations remain small and we assimilate the fibers debonding *prior* to the strain softening onset to a damaging process. With σ_f being the traction at strain softening onset the compliance tensor at that stage can be computed from
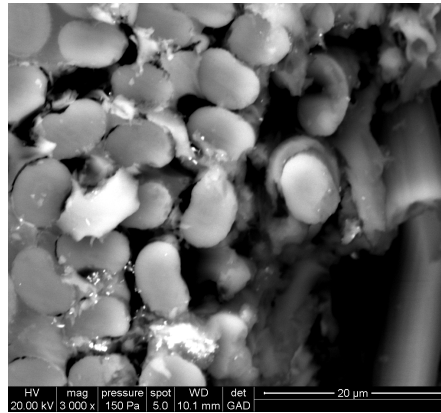
$$L\sigma_f \boldsymbol{e}_X \cdot \mathcal{G} : \boldsymbol{e}_X \otimes \boldsymbol{e}_X = \boldsymbol{u}^{\mathrm{m}}\big|_{\sigma_f} , \qquad (32)$$
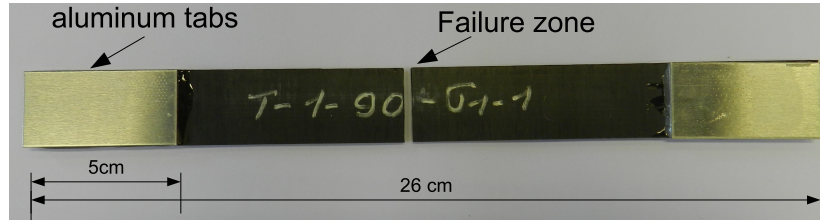
(a) Sample
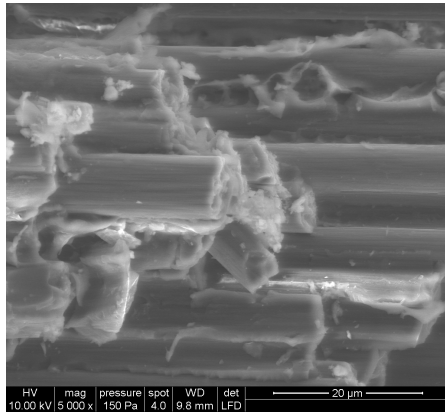
(b) Fracture section

(c) Cross section

Figure 13: Microscopy imaging of a broken sample. (a) Sample. (b) View of the fractured surface (sample center). (c) View of the composite cross section (sample center).

and the cohesive law $\bar{t}$ *vs* u^{M} can thus be deduced directly by projecting in the X-direction the Equations (29-31). The results are reported in Figure 11(b) where it can be seen that the curves coincide for the different cell sizes. Also the energy release rate G_{C} during the meso–crack opening, which corresponds to the area below the cohesive curve, is reported in Table 3. The values obtained are close to the ones resulting from the analysis of Figure 8(e), which justifies the analysis provided herein. Finally Figure 12 represents the stress distribution for a macro opening $\Delta = 1$ μm. The localization is clearly visible on this picture and it can also be seen that the opening at debonding locations tends to close due to the unloading process. For the 8×8–fiber cell the crack is not yet complete through the section as two micro-cracks appear on the top part for one at the bottom part. However at the end of the fracture process only one dominant crack is totally opened $(\Delta^* > \Delta_c)$, which explains why the extracted cohesive law $\bar{t}$ *vs* u^{M} is the same as

for the smaller cells.

Inglis *et al.* [8] have compared the mesoscale responses of plane–strain composites obtained with a mean–field homogenization scheme accounting for debonding and with an asymptotic expansion from finite element cells. In the latter, RVEs with extrinsic cohesive laws at fiber–matrix interfaces are studied. Although their material parameters are different, it is worth noting that the responses they have obtained in Zone II and at the beginning of Zone III qualitatively match our prediction. The main difference with our prediction occurs in Zone III: in our model matrix cracking induces an almost monotonic decrease of the mesoscopic response, while in their model the Zone III exhibits a saw–tooth response with the debonding of inclusions of different sizes corresponding to the different teeth, because ligament cracking is not accounted for.

Finally the predicted fracture behavior, *i.e.* fibers debonding followed by a crack propagation in the matrix, is assessed by microscopic imaging of the fractured sample, see Figure 13(a). Figure 13(b) is a view parallel to the fibers directly obtained from the fractured section and Figure 13(c) is a view perpendicular to the fibers obtained after cutting the sample at its center. Both pictures clearly show an important fiber debonding as well as a crack propagation in the surrounding matrix.

5. Conclusions

In this work the hybrid DG/extrinsic cohesive law framework is extended to the microscale study of composite materials failure. Toward this end micro-structures of UD carbon-fiber reinforced epoxy matrix are discretized using FE. The use of a DG method in combination with the cohesive law presents relevant advantages. On the one hand the drawbacks of the classical insertion of cohesive elements, *i.e.* either the difficulty of inserting them on–the–fly with the extrinsic method or the modification of structure compliance with the intrinsic method, are avoided. On the other hand an efficient parallel implementation is possible which allows fine meshes to be used and thus complex crack path to be captured.

The method is applied to study characteristic micro-volumes of different sizes and thus of different fibers numbers. The irreversible response to the transverse traction of the composite is found to exhibit two stages. *Prior* to the strain softening onset the method captures the debonding process,

which is assimilated to a damaging process. In particular the developed framework predicts a density of dissipated energy resulting from the damage (debonding) that is constant for the different studied cell sizes. During the strain softening phase the initiation and propagation of a main micro–crack is also captured. A corresponding mesoscale cohesive law, which follows the strain softening onset, can then be extracted and is shown to converge for different cell sizes. The predicted behavior is also compared to experimental results obtained from laminate tests and is found to be in good agreement *prior* to fracture.

The method is promising for future use in multi–scale computations, especially as it is shown that cells of reduced sizes can be used, although tests for different loading and fiber orientations should be performed.

Acknowledgment

Appendix A. Material models

Under large deformations the material model is based on the choice of a strain measure and on the definition of an elastic potential of the work-conjugate stress. In the DG weak form (20) the first Piola-Kirchhoff stress tensor $\mathbf{P}$ is considered and its work conjugate-strain measure is the deformation gradient $\mathbf{F}$, with $J = \det(\mathbf{F}) > 0$ its Jacobian.

Two different material behaviors are considered in this work: an anisotropic hyperelastic model for the fibers and a J_2-elastic-plastic model for the matrix. The main equations of these two models are briefly recalled for completeness.

Appendix A.1. Carbon fiber - Transversely isotropic elastic material

A transversely isotropic elastic material is characterized by the following parameters:

$$E_T = E_1 = E_2 \neq E_3 = E_L; \qquad \nu_{TT} = \nu_{12} = \nu_{21} \neq \nu_{13} = \nu_{23} = \nu_{TL};$$
$$G_{LT} = G_{13} = G_{23} = G_3; \qquad G_{TT} = G_{12} = \frac{E}{2(1+\nu_{TT})}, \qquad (A.1)$$

where the subscript "3" refers to the fiber direction. Along this direction the Poisson's ratios are not symmetric but instead satisfy $\nu_{ij}/E_i = \nu_{ji}/E_j$ (no sums). The carbon fibers are modeled using a Neo-Hookean material, which has a strain energy density Ψ dependent on the right Cauchy-Green tensor $\mathbf{C} = \mathbf{F}^T\mathbf{F}$. Considering the transversely isotropic properties of the carbon fibers the neo-Hookean potential $\Psi = \Psi_{iso} + \Psi_{trn}$ includes two parts. The isotropic component is a function of $\mathbf{C}$ via its two invariants

$$\Psi_{iso} = \frac{1}{2}G_{12}(I_1 - 3) - G_{12}\ln J + \frac{1}{2}\lambda\ln^2 J, \qquad (A.2)$$

where $I_1 = \text{tr}(\mathbf{C})$, and where $J^2 = \det(\mathbf{C})$. The orthotropic transversely isotropic component is obtained from a generalization of the model proposed by Bonet and Burton [67][10], and reads

$$\Psi_{trn} = [\alpha_{trn} + 2\beta_{trn}\ln J + \gamma_{trn}(I_4 - 1)](I_4 - 1) - \frac{1}{2}\alpha_{trn}(I_5 - 1) \qquad (A.3)$$

where I_4 and I_5 are the two new pseudo invariants of $\mathbf{C}$ expressed as

$$I_4 = \boldsymbol{A} \cdot \mathbf{C} \cdot \boldsymbol{A} \ \text{ and } \ I_5 = \boldsymbol{A} \cdot \mathbf{C}^2 \cdot \boldsymbol{A}, \qquad (A.4)$$

and where the unit vector $\boldsymbol{A}$ defines the main direction of orthotropy (fibers direction) in the undeformed configuration.

The model parameters of Equations (A.2) and (A.3) are λ, G_{12}, α_{trn}, β_{trn},

---

[10]In the original model $\nu_{TL} = \nu_{TT}$, which is not acceptable for carbon fibers

and γ_{trn} and follow from the measured properties (A.1) as

$$
\begin{aligned}
\lambda &= \frac{E_{\text{T}}\left(\nu_{\text{TT}} + n\nu_{\text{TL}}^2\right)}{m\left(1 + \nu_{\text{TT}}\right)}, \quad G_{12} = \frac{E_{\text{T}}}{2\left(1 + \nu_{\text{TT}}\right)}, \\
\alpha_{\text{trn}} &= G_{12} - G_3, \\
\beta_{\text{trn}} &= \frac{E_{\text{T}}\left[n\nu_{\text{TL}}\left(1 + \nu_{\text{TT}} - \nu_{\text{TL}}\right) - \nu_{\text{TT}}\right]}{4m\left(1 + \nu_{\text{TT}}\right)}, \\
\gamma_{\text{trn}} &= \frac{E_{\text{L}}\left(1 - \nu_{\text{TT}}\right)}{8m} - \frac{\lambda + 2G_{12}}{8} + \frac{\alpha_{\text{trn}}}{2} - \beta_{\text{trn}}, \\
m &= 1 - \nu_{\text{TT}} - 2n\nu_{\text{TL}}^2, \text{ and } n = \frac{E_{\text{L}}}{E_{\text{T}}}.
\end{aligned}
\tag{A.5}
$$

The second Piola-Kirchhoff stress tensor $\mathbf{S} = 2\frac{\partial \Psi}{\partial \mathbf{C}}$ can then be obtained by differentiating the expressions (A.2) and (A.3), leading to

$$
\begin{aligned}
\mathbf{S} = {}& \lambda \ln J \mathbf{C}^{-1} + G_{12}(\mathbf{I} - \mathbf{C}^{-1}) + 2\beta_{\text{trn}}(I_4 - 1)\mathbf{C}^{-1} + 2[\alpha_{\text{trn}} + 2\beta_{\text{trn}}\ln J + \\
& 2\gamma_{\text{trn}}(I_4 - 1)]\boldsymbol{A} \otimes \boldsymbol{A} - \alpha_{\text{trn}}(\mathbf{C} \cdot \boldsymbol{A} \otimes \boldsymbol{A} + \boldsymbol{A} \otimes \mathbf{C} \cdot \boldsymbol{A}),
\end{aligned}
\tag{A.6}
$$

and the first Piola-Kirchhoff stress tensor can readily be obtained from $\mathbf{P} = \mathbf{FS}$.

Appendix A.2. Matrix material - J_2-elastic-plastic material

For an elastic-plastic material, a multiplicative decomposition of the deformation gradient is assumed $\mathbf{F} = \mathbf{F}^e\mathbf{F}^p$, where $\mathbf{F}^e$ and $\mathbf{F}^p$ are the elastic and plastic parts of the deformation gradient, respectively. The material model is based on a hyperelastic formulation with an elastic potential defined as

$$
\Psi(\mathbf{C}^e) = \frac{K}{2}\ln^2 J + \frac{G}{4}[\ln\mathbf{C}^e]^{\text{dev}} : [\ln\mathbf{C}^e]^{\text{dev}},
\tag{A.7}
$$

where $K = \frac{E}{3(1-2\nu)}$ and $G = \frac{E}{2(1+\nu)}$ are the bulk and shear moduli of the material, and where $[\ln\mathbf{C}^e]^{\text{dev}}$ is the deviatoric part of $\ln\mathbf{C}^e$. The defined elastic potential can only explicitly depends on the elastic deformation through the elastic right Cauchy strain tensor $\mathbf{C}^e = \mathbf{F}^{e\text{T}}\mathbf{F}^e$. One can thus derive the first Piola-Kirchhoff stress tensor $\mathbf{P} = 2\mathbf{F}\frac{\partial \Psi}{\partial \mathbf{C}}$ and the Cauchy stress tensor $\boldsymbol{\sigma} = J^{-1}\mathbf{P}\mathbf{F}^{\text{T}}$

$$
\boldsymbol{\sigma} = p'\mathbf{I} + J^{-1}\mathbf{F}^e\left[2G\mathbf{C}^{e-1}(\ln\sqrt{\mathbf{C}^e})^{\text{dev}}\right]\mathbf{F}^{e\text{T}},
\tag{A.8}
$$

where $p' = (K \ln J)/J$ is the pressure, and where the second term on the right hand side of Equation (A.8) is the deviatoric part of the Cauchy stress, $\boldsymbol{\sigma}^{\text{dev}}$. This expression is used to evaluate the equivalent von Mises stress $\sigma^{\text{eq}} = \sqrt{\frac{3}{2}\boldsymbol{\sigma}^{\text{dev}} : \boldsymbol{\sigma}^{\text{dev}}}$ required to solve the J_2-flow theory. The plastic flow

$$\mathbf{F}^p_{n+1} = \exp\left(\triangle p \mathbf{N}^p\right) \mathbf{F}^p_n \,, \tag{A.9}$$

is solved using a standard radial return mapping, where p is the equivalent plastic strain and where the normal of the yield surface $\mathbf{N}^p = \frac{3}{2}\frac{\boldsymbol{\sigma}^{\text{dev}}}{\sigma^{\text{eq}}}$ is calculated from the elastic predictor. More details can be found in the framework proposed by Cuitiño and Ortiz [68].

Appendix B. Formulation of the finite element forces

For a volume element, the inertial forces, internal bulk forces and external forces at node a can be readily obtained directly from the equation (20) as

$$\sum_{b=1}^{N} \mathbf{M}_{ab}\ddot{\boldsymbol{u}}_b = \sum_{b=1}^{N} \int_{\Omega_0} \rho_0 N_a N_b dV \, \ddot{\boldsymbol{u}}_b \,, \tag{B.1}$$

$$\mathbf{f}_{\text{int}a} = \int_{\Omega_0} \mathbf{P}\boldsymbol{\nabla}_0 N_a dV \,, \text{ and} \tag{B.2}$$

$$\mathbf{f}_{\text{ext}a} = \int_{\Omega_0} \rho_0 \mathbf{B} N_a dV + \int_{\Gamma_{0\text{T}}} \mathbf{T} N_a dS \,, \tag{B.3}$$

where $\mathbf{M}_{ab}$ is the mass matrix. Practically we consider 10-node quadratic elements integrated with 4 Gauss points.

The interface forces arising from the DG/CZM formulation are evaluated from the shape functions N_a^+ and N_a^- of the $+$ and $-$ elements sharing the same interface and the same nodes a, although the degrees of freedom at the same node for the two elements are distinct. This is a particularity of the presented implementation, which duplicates the degrees of freedom at a common node instead of duplicating the nodes at common interfaces as this is usually done for cohesive methods. Therefore the expression of the

interface forces for the nodes on the + and − elements reads

$$
\begin{aligned}
\mathbf{f}_{\mathrm{I}a}^{\pm} = \ \pm\ & \int_{\Gamma_{0\mathrm{I}}} (1-\alpha)\,\langle \mathbf{P}\rangle \boldsymbol{N}^- N_a^{\pm}\,dS \\
+\ & \frac{1}{2}\int_{\Gamma_{0\mathrm{I}}} (1-\alpha)\left[\llbracket N_b \boldsymbol{u}_b \rrbracket \otimes \boldsymbol{N}^-\right]: \mathbb{C}^{\pm}\cdot \boldsymbol{\nabla}_0 N_a^{\pm}\,dS \\
\pm\ & \int_{\Gamma_{0\mathrm{I}}} (1-\alpha)\left[\langle \frac{\beta_s}{h_s}\mathbb{C}\rangle : \llbracket N_b \boldsymbol{u}_b \rrbracket \otimes \boldsymbol{N}^-\right]\boldsymbol{N}^- N_a^{\pm}\,dS \\
\pm\ & \int_{\Gamma_{\mathrm{I}}} \alpha\bar{\boldsymbol{t}}^-\left(\llbracket N_b \boldsymbol{u}_b\rrbracket\right) N_a^{\pm}\,ds\,.
\end{aligned}
\tag{B.4}
$$

In the integration above the shape functions N_a explicitly used are the ones of the volume elements and they are evaluated at the integration points of the interface elements. Due to the symmetrization terms all the nodes of the 2 neighboring tetrahedra have force contributions, and not only the nodes of the common interface. The evaluation of (B.4) requires a full 6-point integration at the interface element in order to avoid spurious penetration modes as shown in [42].

References

[1] P. Ladevèze, G. Lubineau, D. Marsal, Towards a bridge between the micro- and mesomechanics of delamination for laminated composites, Composites Science and Technology 66 (6) (2006) 698 – 712, ISSN 0266-3538, doi:10.1016/j.compscitech.2004.12.026, URL http://www.sciencedirect.com/science/article/pii/S0266353804003665.

[2] J. LLorca, C. González, J. M. Molina-Aldareguía, J. Segurado, R. Seltzer, F. Sket, M. Rodríguez, S. Sádaba, R. Muñoz, L. P. Canal, Multiscale Modeling of Composite Materials: a Roadmap Towards Virtual Testing, Advanced Materials 23 (44) (2011) 5130–5147, ISSN 1521-4095, doi:10.1002/adma.201101683.

[3] G. Barenblatt, The Mathematical Theory of Equilibrium Cracks in Brittle Fracture, vol. 7, Elsevier, 55–129, doi:10.1016/S0065-2156(08)70121-2, URL http://www.sciencedirect.com/science/article/B7RNC-4S867RJ-6/2/24d2fbaac93457d 1962.

[4] D. S. Dugdale, Yielding of steel sheets containing slits, Journal of the Mechanics and Physics of Solids 8 (2) (1960) 100–104, ISSN 0022-5096, URL http://www.sciencedirect.com/science/article/B6TXB-46J03KX-2K/2/764967fc069980

[5] A. Hillerborg, M. Modéer, P.-E. Petersson, Analysis of crack formation and crack growth in concrete by means of fracture mechanics and finite elements, Cement and Concrete Research 6 (6) (1976) 773 – 781, ISSN 0008-8846, doi:10.1016/0008-8846(76)90007-7, URL http://www.sciencedirect.com/science/article/pii/0008884676900077.

[6] A. Needleman, A continuum model for void nucleation by inclusion debonding, Journal of Applied Mechanics 54 (3) (1987) 525–531, doi:10.1115/1.3173064, URL http://link.aip.org/link/?AMJ/54/525/1.

[7] V. Tvergaard, Effect of fibre debonding in a whisker-reinforced metal, Materials Science and Engineering: A 125 (2) (1990) 203 – 213, ISSN 0921-5093, doi:10.1016/0921-5093(90)90170-8, URL http://www.sciencedirect.com/science/article/pii/0921509390901708.

[8] H. M. Inglis, P. H. Geubelle, K. Matouˇs, H. Tan, Y. Huang, Cohesive modeling of dewetting in particulate composites: micromechanics vs. multiscale finite element analysis, Mechanics of Materials 39 (6) (2007) 580 – 595, ISSN 0167-6636, doi:10.1016/j.mechmat.2006.08.008, URL http://www.sciencedirect.com/science/article/pii/S0167663606001141.

[9] V. Tvergaard, J. W. Hutchinson, The influence of plasticity on mixed mode interface toughness, Journal of the Mechanics and Physics of Solids 41 (6) (1993) 1119 – 1135, ISSN 0022-5096, doi:10.1016/0022-5096(93)90057-M, URL http://www.sciencedirect.com/science/article/pii/002250969390057M.

[10] V. Tvergaard, J. W. Hutchinson, Toughness of an interface along a thin ductile layer joining elastic solids, Philosophical Magazine A 70 (4) (1994) 641–656, doi:10.1080/01418619408242253, URL http://www.tandfonline.com/doi/abs/10.1080/01418619408242253.

[11] A. Needleman, An analysis of decohesion along an imperfect interface, International Journal of Fracture 42 (1990) 21–40, ISSN 0376-9429, URL http://dx.doi.org/10.1007/BF00018611.

[12] P. P. Camanho, C. G. Dávila, S. T. Pinho, Fracture analysis of composite co-cured structural joints using decohesion elements, Fatigue & Fracture of Engineering Materials & Structures 27 (9) (2004) 745–757, ISSN 1460-2695, doi:10.1111/j.1460-2695.2004.00695.x.

[13] M. C. Miron, D. M. Constantinescu, Strain fields at an interface crack in a sandwich composite, Mechanics of Materials 43 (12) (2011) 870 – 884, ISSN 0167-6636, doi:10.1016/j.mechmat.2011.10.002, URL http://www.sciencedirect.com/science/article/pii/S0167663611001839.

[14] P. H. Geubelle, J. S. Baylor, Impact-induced delamination of composites: a 2D simulation, Composites Part B: Engineering 29 (5) (1998) 589 – 602, ISSN 1359-8368, doi:10.1016/S1359-8368(98)00013-4, URL http://www.sciencedirect.com/science/article/pii/S1359836898000134.

[15] A. Pantano, R. C. Averill, A mesh-independent interface technology for simulation of mixed-mode delamination growth, International Journal of Solids and Structures 41 (14) (2004) 3809 – 3831, ISSN 0020-7683, doi:10.1016/j.ijsolstr.2004.02.018, URL http://www.sciencedirect.com/science/article/pii/S0020768304000745.

[16] A. Turon, C. G. Dávila, P. P. Camanho, J. Costa, An engineering solution for mesh size effects in the simulation of delamination using cohesive zone models, Engineering Fracture Mechanics 74 (10) (2007) 1665 – 1682, ISSN 0013-7944, doi:10.1016/j.engfracmech.2006.08.025, URL http://www.sciencedirect.com/science/article/pii/S0013794406003808.

[17] V. Tvergaard, Crack growth predictions by cohesive zone model for ductile fracture, Journal of the Mechanics and Physics of Solids 49 (9) (2001) 2191–2207, ISSN 0022-5096, doi:10.1016/S0022-5096(01)00030-8, URL http://www.sciencedirect.com/science/article/B6TXB-43RTTVV-P/2/f3f973c37035969

[18] X.-P. Xu, A. Needleman, Void nucleation by inclusion debonding in a crystal matrix, Modelling Simul. Mater. Sci. Eng. 1 (1993) 111–132, doi:10.1088/0965-0393/1/2/001.

[19] V. Tvergaard, J. W. Hutchinson, The relation between crack growth resistance and fracture process parameters in elastic-plastic solids, Journal of the Mechanics and Physics of Solids 40 (6) (1992)

1377 – 1397, ISSN 0022-5096, doi:10.1016/0022-5096(92)90020-3, URL http://www.sciencedirect.com/science/article/pii/0022509692900203.

[20] O. Nguyen, M. Ortiz, Coarse-graining and renormalization of atomistic binding relations and universal macroscopic cohesive behavior, Journal of the Mechanics and Physics of Solids 50 (8) (2002) 1727 – 1741, ISSN 0022-5096, doi:10.1016/S0022-5096(01)00133-8, URL http://www.sciencedirect.com/science/article/pii/S0022509601001338.

[21] X.-P. Xu, A. Needleman, Numerical simulations of fast crack growth in brittle solids, Journal of the Mechanics and Physics of Solids 42 (9) (1994) 1397 – 1434, ISSN 0022-5096, doi:10.1016/0022-5096(94)90003-5, URL http://www.sciencedirect.com/science/article/pii/0022509694900035.

[22] S. H. Song, G. H. Paulino, W. G. Buttlar, A bilinear cohesive zone model tailored for fracture of asphalt concrete considering viscoelastic bulk material, Engineering Fracture Mechanics 73 (18) (2006) 2829 – 2848, ISSN 0013-7944, doi:10.1016/j.engfracmech.2006.04.030, URL http://www.sciencedirect.com/science/article/pii/S0013794406001755.

[23] N. Blal, L. Daridon, Y. Monerie, S. Pagano, Criteria on the artificial compliance inherent to the intrinsic cohesive zone, Comptes Rendus Mécanique 339 (12) (2011) 789 – 795, ISSN 1631-0721, doi:10.1016/j.crme.2011.10.001, URL http://www.sciencedirect.com/science/article/pii/S1631072111001677.

[24] P. D. Zavattieri, H. D. Espinosa, Grain level analysis of crack initiation and propagation in brittle materials, Acta Materialia 49 (20) (2001) 4291 – 4311, ISSN 1359-6454, doi:10.1016/S1359-6454(01)00292-0, URL http://www.sciencedirect.com/science/article/pii/S1359645401002920.

[25] G. T. Camacho, M. Ortiz, Computational modelling of impact damage in brittle materials, International Journal of Solids and Structures 33 (20-22) (1996) 2899–2938, ISSN 0020-7683, doi:10.1016/0020-7683(95)00255-3, URL http://www.sciencedirect.com/science/article/B6VJS-3VTSPVJ-3/2/98fe3c31d0cee8e

[26] M. Ortiz, A. Pandolfi, Finite-Deformation Irreversible Cohesive Elements for Three-Dimensional Crack Propagation Analysis, International Journal for Numerical Methods in Engineering 44 (9)

(1999) 1267–1282, ISSN 1097-0207, doi:10.1002/(SICI)1097-0207(19990330)44:9<1267::AID-NME486>3.0.CO;2-7, URL `http://dx.doi.org/10.1002/(SICI)1097-0207(19990330)44:9<1267::AID-NME486>3.0.`

[27] A. Pandolfi, P. R. Guduru, M. Ortiz, A. J. Rosakis, Three dimensional cohesive-element analysis and experiments of dynamic fracture in C300 steel, International Journal of Solids and Structures 37 (27) (2000) 3733 – 3760, ISSN 0020-7683, doi:10.1016/S0020-7683(99)00155-9, URL `http://www.sciencedirect.com/science/article/pii/S0020768399001559`.

[28] I. Arias, J. Knap, V. B. Chalivendra, S. Hong, M. Ortiz, A. J. Rosakis, Numerical modelling and experimental validation of dynamic fracture events along weak planes, Computer Methods in Applied Mechanics and Engineering 196 (37-40) (2007) 3833 – 3840, ISSN 0045-7825, doi:10.1016/j.cma.2006.10.052, URL `http://www.sciencedirect.com/science/article/pii/S0045782507001107`.

[29] J. F. Molinari, G. Gazonas, R. Raghupathy, A. Rusinek, F. Zhou, The cohesive element approach to dynamic fragmentation: the question of energy convergence, International Journal for Numerical Methods in Engineering 69 (3) (2007) 484–503, ISSN 1097-0207, URL `http://dx.doi.org/10.1002/nme.1777`.

[30] A. Pandolfi, M. Ortiz, An Efficient Adaptive Procedure for Three-Dimensional Fragmentation Simulations, Engineering with Computers 18 (2) (2002) 148–159, ISSN 0177-0667, doi:10.1007/s003660200013, URL `http://dx.doi.org/10.1007/s003660200013`.

[31] A. Mota, J. Knap, M. Ortiz, Fracture and fragmentation of simplicial finite element meshes using graphs, International Journal for Numerical Methods in Engineering 73 (11) (2008) 1547–1570, ISSN 1097-0207, doi:10.1002/nme.2135, URL `http://dx.doi.org/10.1002/nme.2135`.

[32] G. Paulino, W. Celes, R. Espinha, Z. Zhang, A general topology-based framework for adaptive insertion of cohesive elements in finite element meshes, Engineering with Computers 24 (2008) 59–78, ISSN 0177-0667, doi:10.1007/s00366-007-0069-7, URL `http://dx.doi.org/10.1007/s00366-007-0069-7`.

[33] N. Moës, J. Dolbow, T. Belytschko, A finite element method for crack growth without remeshing, International Journal for Numerical Methods in Engineering 46 (1) (1999) 131–150, ISSN 1097-0207, doi:10.1002/(SICI)1097-0207(19990910)46:1<131::AID-NME726>3.0.CO;2-J, URL `http://dx.doi.org/10.1002/(SICI)1097-0207(19990910)46:1<131::AID-NME726>3.0.C0`

[34] N. Moës, T. Belytschko, Extended finite element method for cohesive crack growth, Engineering Fracture Mechanics 69 (7) (2002) 813–833, ISSN 0013-7944, doi:10.1016/S0013-7944(01)00128-X, URL `http://www.sciencedirect.com/science/article/B6V2R-457VNPR-3/2/6a76fcf28df8e4C`

[35] F. Armero, C. Linder, Numerical simulation of dynamic fracture using finite elements with embedded discontinuities, International Journal of Fracture 160 (2009) 119–141, ISSN 0376-9429, doi:10.1007/s10704-009-9413-9, URL `http://dx.doi.org/10.1007/s10704-009-9413-9`.

[36] R. de Borst, M. A. Gutiérrez, G. N. Wells, J. J. C. Remmers, H. Askes, Cohesive-zone models, higher-order continuum theories and reliability methods for computational failure analysis, International Journal for Numerical Methods in Engineering 60 (1) (2004) 289–315, ISSN 1097-0207, doi:10.1002/nme.963, URL `http://dx.doi.org/10.1002/nme.963`.

[37] J. Mergheim, E. Kuhl, P. Steinmann, A hybrid discontinuous Galerkin/interface method for the computational modelling of failure, Communications in Numerical Methods in Engineering 20 (7) (2004) 511–519, URL `http://dx.doi.org/10.1002/cnm.689`.

[38] R. Radovitzky, A. Seagraves, M. Tupek, L. Noels, A scalable 3D fracture and fragmentation algorithm based on a hybrid, discontinuous Galerkin, cohesive element method, Computer Methods in Applied Mechanics and Engineering 200 (14) (2011) 326–344, ISSN 0045-7825, doi:10.1016/j.cma.2010.08.014, URL `http://www.sciencedirect.com/science/article/pii/S0045782510002471`.

[39] M. Prechtel, G. Leugering, P. Steinmann, M. Stingl, Towards optimization of crack resistance of composite materials by adjustment of fiber shapes, Engineering Fracture Mechanics 78 (6) (2011) 944

– 960, ISSN 0013-7944, doi:10.1016/j.engfracmech.2011.01.007, URL
`http://www.sciencedirect.com/science/article/pii/S0013794411000117`.

[40] L. Noels, R. Radovitzky, A general discontinuous Galerkin method
for finite hyperelasticity. Formulation and numerical applications,
International Journal for Numerical Methods in Engineering
68 (1) (2006) 64–97, ISSN 1097-0207, doi:10.1002/nme.1699, URL
`http://dx.doi.org/10.1002/nme.1699`.

[41] A. Ten Eyck, A. Lew, Discontinuous Galerkin methods for non-linear
elasticity, International Journal for Numerical Methods in Engineering
67 (9) (2006) 1204–1243, ISSN 1097-0207, doi:10.1002/nme.1667, URL
`http://dx.doi.org/10.1002/nme.1667`.

[42] L. Noels, R. Radovitzky, An explicit discontinuous Galerkin method
for non-linear solid dynamics: Formulation, parallel implementation
and scalability properties, International Journal for Numerical Meth-
ods in Engineering 74 (9) (2008) 1393–1420, ISSN 1097-0207, doi:
10.1002/nme.2213, URL `http://dx.doi.org/10.1002/nme.2213`.

[43] A. Lew, A. Ten Eyck, R. Rangarajan, Some Applications of Dis-
continuous Galerkin Methods in Solid Mechanics, IUTAM Sympo-
sium on Theoretical, Computational and Modelling Aspects of In-
elastic Media (2008) 227–236doi:10.1007/978-1-4020-9090-5_21, URL
`http://dx.doi.org/10.1007/978-1-4020-9090-5_21`.

[44] A. Ten Eyck, F. Celiker, A. Lew, Adaptive stabilization of dis-
continuous Galerkin methods for nonlinear elasticity: Motiva-
tion, formulation, and numerical examples, Computer Meth-
ods in Applied Mechanics and Engineering 197 (45-48) (2008)
3605–3622, ISSN 0045-7825, doi:10.1016/j.cma.2008.02.020, URL
`http://www.sciencedirect.com/science/article/B6V29-4RY6WKK-1/2/c484a571e4c532a`

[45] G. Becker, L. Noels, A fracture framework for Euler-Bernoulli beams
based on a full discontinuous Galerkin formulation/extrinsic cohe-
sive law combination, International Journal for Numerical Meth-
ods in Engineering 85 (10) (2011) 1227–1251, ISSN 1097-0207, doi:
10.1002/nme.3008, URL `http://dx.doi.org/10.1002/nme.3008`.

[46] G. Becker, C. Geuzaine, L. Noels, A one Field Full Discontinuous Galerkin Method for Kirchhoff-Love Shells Applied to Fracture Mechanics, Computer Methods in Applied Mechanics and Engineering 200 (4546) (2011) 3223–3241, ISSN 0045-7825, doi:10.1016/j.cma.2011.07.008, URL http://www.sciencedirect.com/science/article/pii/S0045782511002490.

[47] G. Becker, L. Noels, A full discontinuous Galerkin formulation of nonlinear Kirchhoff-Love shells: elasto-plastic finite deformations, parallel computation & fracture applications, International Journal for Numerical Methods in Engineering 93 (1) (2013) 80–117, ISSN 1097-0207, doi: 10.1002/nme.4381, URL http://dx.doi.org/10.1002/nme.4381.

[48] I. Gitman, H. Askes, L. Sluys, Representative volume: Existence and size determination, Engineering Fracture Mechanics 74 (16) (2007) 2518 – 2534, ISSN 0013-7944, doi:10.1016/j.engfracmech.2006.12.021, URL http://www.sciencedirect.com/science/article/pii/S0013794406004772.

[49] C. Pelissou, J. Baccou, Y. Monerie, F. Perales, Determination of the size of the representative volume element for random quasi-brittle composites, International Journal of Solids and Structures 46 (14-15) (2009) 2842 – 2855, ISSN 0020-7683, doi:10.1016/j.ijsolstr.2009.03.015, URL http://www.sciencedirect.com/science/article/pii/S0020768309001334.

[50] V. P. Nguyen, O. Lloberas-Valls, M. Stroeven, L. J. Sluys, On the existence of representative volumes for softening quasi-brittle materials – A failure zone averaging scheme, Computer Methods in Applied Mechanics and Engineering 199 (45-48) (2010) 3028 – 3038, ISSN 0045-7825, doi:10.1016/j.cma.2010.06.018, URL http://www.sciencedirect.com/science/article/pii/S0045782510001854.

[51] E. W. C. Coenen, V. G. Kouznetsova, M. G. D. Geers, Novel boundary conditions for strain localization analyses in microstructural volume elements, International Journal for Numerical Methods in Engineering 90 (1) (2012) 1–21, ISSN 1097-0207, doi:10.1002/nme.3298, URL http://dx.doi.org/10.1002/nme.3298.

[52] E. W. C. Coenen, V. G. Kouznetsova, M. G. D. Geers, Multi-scale continuous-discontinuous framework for computational-homogenization-localization, Journal of the Mechanics and Physics of Solids 60 (8) (2012)

1486 – 1507, ISSN 0022-5096, doi:10.1016/j.jmps.2012.04.002, URL `http://www.sciencedirect.com/science/article/pii/S0022509612000749`.

[53] A. Jérusalem, Continuum modeling of the reverse HallPetch effect in nanocrystalline metals under uniaxial tension: how many grains in a finite element model?, Philosophical Magazine Letters 91 (9) (2011) 599–609, ISSN 0950-0839, doi:10.1080/09500839.2011.598478.

[54] C. V. Verhoosel, J. J. C. Remmers, M. A. Gutiérrez, R. de Borst, Computational homogenization for adhesive and cohesive failure in quasibrittle solids, International Journal for Numerical Methods in Engineering 83 (8-9) (2010) 1155–1179, ISSN 1097-0207, doi:10.1002/nme.2854, URL `http://dx.doi.org/10.1002/nme.2854`.

[55] V. P. Nguyen, M. Stroeven, L. J. Sluys, An enhanced continuous–discontinuous multiscale method for modeling mode-I cohesive failure in random heterogeneous quasi-brittle materials, Engineering Fracture Mechanics 79 (0) (2012) 78 – 102, ISSN 0013-7944, doi:10.1016/j.engfracmech.2011.10.005, URL `http://www.sciencedirect.com/science/article/pii/S0013794411003845`.

[56] G. Leugering, M. Prechtel, P. Steinmann, M. Stingl, A cohesive crack propagation model: Mathematical theory and numerical solution, Communications on Pure and Applied Analysis 12 (2013) 1705–1729, doi:10.3934/cpaa.2013.12.1705, URL `http://www.aimsciences.org/journals/displayArticlesnew.jsp?paperID=7926`.

[57] A. Seagraves, R. Radovitzky, Advances in Cohesive Zone Modeling of Dynamic Fracture, in: A. Shukla, G. Ravichandran, Y. D. Rajapakse (Eds.), Dynamic Failure of Materials and Structures, Springer US, ISBN 978-1-4419-0446-1, 349–405, 10.1007/978-1-4419-0446-1_12, 2010.

[58] C. Geuzaine, J.-F. Remacle, Gmsh: A 3-D finite element mesh generator with built-in pre- and post-processing facilities, International Journal for Numerical Methods in Engineering 79 (11) (2009) 1309–1331, doi:10.1002/nme.2579, URL `http://dx.doi.org/10.1002/nme.2579`.

[59] G. M. Hulbert, J. Chung, Explicit time integration algorithms for structural dynamics with optimal numerical dissipation, Computer Methods in Applied Mechanics and Engineering 137 (2) (1996)

175 – 188, ISSN 0045-7825, doi:10.1016/S0045-7825(96)01036-5, URL
http://www.sciencedirect.com/science/article/B6V29-3WFNRDY-5/2/2ec79b924e3dd1b

[60] G. Karypis, V. Kumar, A Fast and High Quality Multilevel Scheme for
Partitioning Irregular Graphs, SIAM Journal on Scientific Computing
20 (1) (1998) 359–392.

[61] I. Dooley, S. Mangala, L. Kale, P. H. Geubelle, Parallel
Simulations of Dynamic Fracture Using Extrinsic Cohesive
Elements, Journal of Scientific Computing 39 (2009) 144–
165, ISSN 0885-7474, doi:10.1007/s10915-008-9254-0, URL
http://link.springer.com/article/10.1007%2Fs10915-008-9254-0?LI=true.

[62] J. Byström, Optimal design of a long and slender com-
pressive strut, The International Journal of Multiphysics
3 (2009) 235–257, doi:10.1260/175095409788922275, URL
http://dx.doi.org/10.1260/175095409788922275.

[63] N. Sato, T. Kurauchi, O. Kamigaito, Fracture mecha-
nism of unidirectional carbon-fibre reinforced epoxy resin
composite, Journal of Materials Science 21 (1986) 1005–
1010, ISSN 0022-2461, doi:10.1007/BF01117386, URL
http://dx.doi.org/10.1007/BF01117386.

[64] A. C. Moloney, H. H. Kausch, T. Kaiser, H. R. Beer, Pa-
rameters determining the strength and toughness of partic-
ulate filled epoxide resins, Journal of Materials Science 22
(1987) 381–393, ISSN 0022-2461, doi:10.1007/BF01160743, URL
http://dx.doi.org/10.1007/BF01160743.

[65] Y. Jia, W. Yan, L. Hong-Yuan, Carbon fibre pullout under the
influence of residual thermal stresses in polymer matrix com-
posites, Computational Materials Science 62 (0) (2012) 79 –
86, ISSN 0927-0256, doi:10.1016/j.commatsci.2012.05.019, URL
http://www.sciencedirect.com/science/article/pii/S092702561200290X.

[66] F. Zhou, J.-F. c. Molinari, Stochastic fracture of ceram-
ics under dynamic tensile loading, International Journal
of Solids and Structures 41 (22-23) (2004) 6573 – 6596,

ISSN   0020-7683,   doi:10.1016/j.ijsolstr.2004.05.029,   URL
http://www.sciencedirect.com/science/article/pii/S0020768304002562.

[67] J. Bonet, A. J. Burton, A simple orthotropic, transversely isotropic
hyperelastic constitutive equation for large strain computations, Com-
puter Methods in Applied Mechanics and Engineering 162 (1-4) (1998)
151 – 164, ISSN 0045-7825, doi:10.1016/S0045-7825(97)00339-3, URL
http://www.sciencedirect.com/science/article/pii/S0045782597003393.

[68] A. Cuitiño, M. Ortiz, A material-independent method for ex-
tending stress update algorithms from small-strain plasticity to fi-
nite plasticity with multiplicative kinematics, Engineering Computa-
tions 9 (1992) 437–451, ISSN 0264-4401, doi:10.1108/eb023876, URL
http://dx.doi.org/10.1108/eb023876.